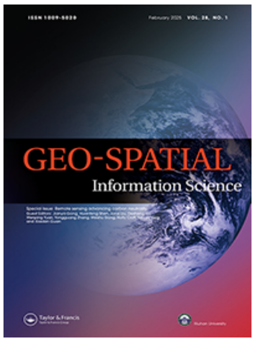

Geo-spatial Information Science

ISSN: (Print) (Online) Journal homepage: www.tandfonline.com/journals/tgsi20

Mapping ground deformation in the northern Yangtze River estuary using improved MT-InSAR based on ICA and non-stationary analysis

Zhijie Zhang, Songbo Wu, Guoqiang Shi, Xiaoli Ding, Chaoying Zhao, Bochen Zhang, Liang Chen & Zhong Lu

To cite this article: Zhijie Zhang, Songbo Wu, Guoqiang Shi, Xiaoli Ding, Chaoying Zhao, Bochen Zhang, Liang Chen & Zhong Lu (17 Jan 2025): Mapping ground deformation in the northern Yangtze River estuary using improved MT-InSAR based on ICA and non-stationary analysis, Geo-spatial Information Science, DOI: 10.1080/10095020.2024.2443484

To link to this article: https://doi.org/10.1080/10095020.2024.2443484

GEO-SPATIAL INFORMATION SCIENCE
https://doi.org/10.1080/10095020.2024.2443484

Taylor & Francis
Taylor & Francis Group

Mapping ground deformation in the northern Yangtze River estuary using improved MT-InSAR based on ICA and non-stationary analysis

Zhijie Zhang[a,b], Songbo Wu[a,f], Guoqiang Shi[a,f], Xiaoli Ding[a,f], Chaoying Zhao[b], Bochen Zhang[c], Liang Chen[d] and Zhong Lu[e]

[a]Department of Land Surveying and Geo-Informatics, and Research Institute for Land and Space, The Hong Kong Polytechnic University, Hong Kong, China; [b]College of Geology Engineering and Geomatics, Chang'an University, Xi'an, China; [c]MNR Key Laboratory for Geo-Environmental Monitoring of Great Bay Area, College of Civil and Transportation Engineering, Shenzhen University, Shenzhen, China; [d]Nantong Surveying and Mapping Research Institute Co, Ltd, Nantong, China; [e]Roy M. Huffington Department of Earth Sciences, South Methodist University, Dallas, USA; [f]Shenzhen Research Institute, The Hong Kong Polytechnic University, Shenzhen, China

ABSTRACT
Coastal regions are increasingly vulnerable to ground deformation hazards, which can cause structural damage and amplify flood risks. Accurately monitoring the evolution of such deformation is crucial for hazard assessment. However, the precision of multi-temporal interferometric synthetic aperture radar (MT-InSAR), a powerful geodetic technique for mapping ground deformation, is often compromised by the atmospheric phase screen (APS) effect. This is more serious in coastal zones, where it can bias the detection of deformation turning points and mislead the interpretation. In this paper, we introduce a novel approach that designs a non-stationarity test for independent component analysis (ICA) to effectively separate the APS and deformation phase components in MT-InSAR applications. Through simulated experiments, the proposed method demonstrated a 50% improvement in deformation accuracy and can effectively track deformation progression. We validated the new method with a case study in Nantong, a coastal region along the northern Yangtze River estuary in China, using Sentinel-1 data from 2015 to 2023. The proposed method retrieved the ground deformation over Nantong with a root-mean-square-error (RMSE) of less than 5.6 mm when compared to ground leveling measurements, which surpasses the traditional MT-InSAR methods. The study results identified diverse ground deformation patterns in Nantong, with deformation rates ranging from −56.3 to 45.9 mm/year, attributed to groundwater extraction, urbanization activities, and land reclamation efforts. The study also highlights the significant coastal accretion and land reclamation processes in the study area, demonstrating the potential capability of the MT-InSAR technique in detecting coastal erosion detection and informing land reservation.

ARTICLE HISTORY
Received 28 August 2024
Accepted 12 December 2024

KEYWORDS
Atmospheric phase screen (APS) mitigation; coastal deformation monitoring; multi-temporal interferometric synthetic aperture radar (MT-InSAR); independent component analysis (ICA); non-stationary test

1. Introduction

Coastal regions worldwide are vulnerable to a range of hazards, which are exacerbated by the combined effects of natural dynamics and human activities (Herrera-García et al. 2021; Shirzaei et al. 2021). One such hazard, ground deformation, can lead to significant threats including structural damage, increased flood risk, and other related issues (Dinar et al. 2021; Zhang et al. 2019). For instance, human-induced factors are significant contributors, accounting for approximately 76.92% of deformation cases (Bagheri-Gavkosh et al. 2021). Numerous major cities worldwide are experiencing ground subsidence hazards due to activities, such as groundwater extraction, construction activities, and land reclamation projects (Herrera-García et al. 2021; Ma et al. 2024; Zhang et al. 2021; Zhao et al. 2019). Given these impacts, accurate monitoring of the evolution of ground deformation is crucial for effective risk assessment and development of early hazard warning systems.

Traditional ground deformation monitoring methods, such as leveling and GNSS, are limited by their high labor costs and restricted spatial coverage (Huang et al. 2017). In contrast, multi-temporal interferometric synthetic aperture radar (MT-InSAR) is a powerful geodesy technique that can detect ground deformation from space and offer distinct advantages over traditional monitoring techniques, with wide coverage, high spatial resolution, and regular observation (Kim et al. 2015; Schlögl, Widhalm, and Avian 2021; Xue et al. 2020). However, the accuracy of the MT-InSAR-derived deformation is affected by the atmospheric phase screen (APS) effect, particularly in coastal areas (Falabella et al. 2024; Hanssen 2001;

CONTACT Songbo Wu song.bo.wu@connect.polyu.hk
Supplemental data for this article can be accessed online at https://doi.org/10.1080/10095020.2024.2443484

Shi et al. 2022; Zebker, Rosen, and Hensley 1997). The APS effect can even introduce errors of up to 20 cm in deformation measurements (Maubant et al. 2020). Therefore, successful mitigation of the APS effect is essential for accurate ground deformation monitoring using MT-InSAR technology (Liao et al. 2013; Rouet-Leduc et al. 2021).

The past two decades have witnessed significant developments in APS mitigation in MT-InSAR. A common method for this purpose is spatiotemporal filtering, which exploits the distinct spatiotemporal properties of APS and deformation (Berardino et al. 2002; Ferretti and Prati 2000). Another method is a model-based approach that employs an empirical or a mathematical model (Bekaert, Hooper, and Wright 2015; Cao et al. 2018, Liang et al., 2019a; Liao et al. 2013). Auxiliary data, such as tropospheric delays derived from GNSS data, have also been used to compensate for the APS effect (ElGharbawi and Tamura 2014; Jung, Kim, and Park 2014; Ding, and Liu 2004; Li et al. 2006; Yu, Li, and Penna 2018). Despite the success of these methods in reducing the effects of APS, significant limitations still exist. For instance, the turning point of the deformation time series, which is important for identifying the evaluation of potential hazards, can be misidentified because of spatiotemporal filtering. The model-based approach may not work well if the accuracy of the model is inadequate and the spatial resolution of auxiliary data is typically very low (Kirui et al. 2021).

In recent years, independent component analysis (ICA) as an effective method has been widely used in MT-InSAR to mitigate the APS effect (Ebmeier 2016; Shi et al. 2022) to separate deformation trends from seasonality (Rigamonti et al. 2023; Xia et al. 2024), based on the statistical characteristics of the individual signals. ICA is a technique that separates non-Gaussian, statistically independent latent signals from mixed signals, which can be divided into spatial ICA (sICA) and temporal ICA (tICA). In MT-InSAR applications, ICA treats each interferogram (IFG) as a linear combination of mixed signals. sICA focuses on spatial independence, suitable for applications to separate the signals with unique pattern. It often requiring prior knowledge of deformation patterns for accurate ICA component identification. tICA emphasizes temporal independence, that captures the distinct temporal characteristics of deformation time series and typically requires dimensionality reduction. Despite their utility in MT-InSAR applications, both methods struggle to automatically identify ICA components related to the deformation signal. The accuracy of retrieved deformation time series can be biased if the deformation ICA sources are inadequately chosen, especially when the characteristics of the deformation are not known in advance (Gaddes, Hooper, and Bagnardi 2019).

In this paper, we propose an improved ICA method for processing MT-InSAR data that automatically identifies deformation source components and effectively separates them from the APS effect. The proposed method uses the single-master unwrapped IFG stack as the initial input for sICA. To identify the deformation related component based on the mixing matrix derived from sICA, we have developed a non-stationarity test (NST) procedure. This procedure automatically evaluates each independent data source, enabling the selection of the deformation-related components by taking advantage of the distinguished characteristics of APS and deformation in spatiotemporal domain. In addition, the effect of spatial correlation blocking is also considered to enhance the robustness of the analysis. We evaluated the effectiveness of the proposed method in mitigating the APS effect and identifying deformation turning points through a series of simulated experiments and compared with two existing MT-InSAR methods. For further assessment, we applied our method to monitor ground deformation over rapidly urbanizing Nantong City, located on the northern bank of the Yangtze River Estuary, using Sentinel-1 SAR data from 2015 to 2023. Various sources of ground deformation related to construction activities, groundwater withdrawal, and coastal accretion/reclamation were identified and discussed in detail. The rest of this paper is organized as follows: the methodology of the proposed method is introduced in Section 2. Section 3 and Section 4 present comparison experiments with simulated and real datasets. Section 5.5 provides a comprehensive discussion and highlights new findings. Section 6 gives the conclusion of the paper.

2. Methodology

2.1. MT-InSAR assisted with ICA

ICA can separate multiple non-Gaussian and statistically independent latent signals, assuming that the mixed signal is a linear combination of individual signals. The ICA model can be expressed as a linear transformation,

$$\boldsymbol{X} = \boldsymbol{A}\boldsymbol{S} \tag{1}$$

where $\boldsymbol{X}$ is the matrix of the mixed signal that can be observed; $\boldsymbol{S}$ is the source matrix of individual signals, each row corresponds to an independent latent signal source; $\boldsymbol{A}$ is the mixing matrix where each column represents the mixing coefficients of an independent signal source. The goal of ICA is to estimate the mixing matrix $\boldsymbol{A}$ and the source matrix $\mathbf{S}$ from the observed matrix $\boldsymbol{X}$. To do this, it needs to retrieve the unmixing matrix $\boldsymbol{W}$, as shown in Equation (2) where $\boldsymbol{W} = \boldsymbol{A}^{-1}$. In this study, one of the most widely used ICA algorithms, the Fast Independent Component Analysis (FastICA) (Hyvarinen 1999), will be adopted,

$$\hat{S} = \boldsymbol{W}\boldsymbol{X} \tag{2}$$

Once the mixing matrix ($\boldsymbol{A}$) and independent sources ($\overset{\wedge}{\mathbf{S}}$) have been obtained, the independent signals can be identified and reconstructed. In general, ICA can be classified into two main types: sICA and tICA. They differ in their emphasis on different spatiotemporal characteristics of the independent signals when organizing the input data ($\boldsymbol{X}$). sICA is employed when the main objective is to separate the sources based on spatial independence. It is particularly useful in applications where the spatial characteristics or distributions of the sources are the focus, regardless of their temporal behavior. In contrast, tICA focuses on temporal dynamics, identifying and separating sources based on their temporal behaviors without restricting the spatial characteristics.

Given N SAR images, M IFGs can be generated, where $\frac{N-1}{2} < M < \frac{N(N-1)}{2}$. It is assumed that all the IFGs are phase unwrapped without error. The interferometric phase of an IFG can be expressed as a linear combination of various components,

$$\begin{aligned} &\varphi_{IFG}^{i,j} = \varphi_{Flat}^{i,j} + \varphi_{DEM}^{i,j} + \varphi_{APS}^{i,j} + \varphi_{Defo}^{i,j} + \varphi_{Noise}^{i,j} \\ &i,j \in \{1,2,3,\ldots,N; i<j\} \end{aligned} \tag{3}$$

where $\varphi_{Flat}^{i,j}$ and $\varphi_{DEM}^{i,j}$ are the Earth curvature and topographic phase components of IFG generated with (i)-th, and (j)-th SAR acquisitions, respectively; $\varphi_{APS}^{i,j}$ and $\varphi_{Defo}^{i,j}$ are the APS and deformation phase components; $\varphi_{Noise}^{i,j}$ is the noise. $\varphi_{Flat}^{i,j}$ and $\varphi_{DEM}^{i,j}$ can be compensated using accurate orbital information, external DEM product, and error correction models (Fattahi and Amelung 2013; Hanssen 2001; Hou et al. 2024; Zhang et al. 2014). Therefore, Equation (3) can be simplified as,

$$\varphi_{IFG}^{i,j} = \varphi_{APS}^{i,j} + \varphi_{Defo}^{i,j} + \varphi_{Noise}^{i,j} \tag{4}$$

In the spatial domain, APS and deformation are non-Gaussian and mutually independent. Therefore, the sICA can be used to separate them (Ebmeier 2016; Gaddes et al. 2018). In this context, each unwrapped IFG is considered as a mixed input for the sICA. When multiple IFGs are available, all of them capture the same deformation characteristics spatially, e.g. volcanic motion. It is possible to separate the deformation source from the APS based on Equation (1) (Gaddes et al. 2018). However, sICA lacks temporal constraints, resulting in the identified spatial components varying over time. Prior information about the deformation is necessary to accurately identify the deformation component.

tICA has also been used in MTInSAR to distinguish different types of temporal deformation (Chaussard et al. 2017), in which the time series of IFGs compensated for the APS (Kirui et al. 2021) are temporally organized and considered as the input for tICA,

$$\begin{aligned} &\varphi_{IFG}^{1,j,p} = \varphi_{Defo}^{1,j,p} + \varphi_{Noise}^{1,j,p} \\ &p = 1,2,3,\ldots,P \end{aligned}$$

with

$$\varphi_{Defo} = \sum_{k=1}^{k=m} \varphi_{type}^{k} \tag{5}$$

where p is the pixel number of an IFG; φ_{type}^{k} represents a deformation type, e.g. periodical, linear, etc.; m is the number of the independent deformation types. Since tICA is not spatially constrained, the separated independent components may each display distinct spatial patterns, reflecting different types of deformation. To manage the dimensionality of the input signals to improve the efficiency of the tICA, it is common to perform dimensionality reduction to the temporally organized data, using e.g. PCA (Gaddes et al. 2018; Shi et al. 2022).

In implementing ICA for separating the APS from the deformation signals in MT-InSAR data processing, there are important challenges, one of which is that manual identification of the independent signals is required (Peng et al. 2022; Wen et al. 2024; Xia et al. 2023). Additionally, it is not always possible to have prior knowledge of the spatial characteristics of ground deformation, especially in a wide region.

2.2. Enhancing ICA with non-stationary test

In this section, we propose an improved ICA method to automatically identify the deformation component in ICA and separate it with APS effects from the MT-InSAR datasets. Since APS signals are of typically low frequency in space but high frequency in time, while the deformation signals tend to be of low frequency in both space and time (Ferretti, Prati, and Rocca 2001). The timing and duration of a deformation event are often unpredictable. When the deformation amplitude is small and the event lasts for a short time, its signal in an IFG may be obscured by atmospheric phase noise. To better distinguish between the APS and the deformation signals, single-master unwrapped IFG stack, referring to the first SAR acquisition, $\varphi_{IFG}^{1,j}$, is spatially organized as the mixed signal for the sICA,

$$\varphi_{IFG}^{1,j} = \varphi_{APS}^{1,j} + \varphi_{Defo}^{1,j} + \varphi_{Noise}^{1,j} \tag{6}$$

where $\varphi_{APS}^{1,j}$ is the APS phase difference between the first and (j)-th SAR images; $\varphi_{Defo}^{1,j}$ is the deformation accumulated up to the (j)-th image. The number of independent sources is set to match the number of

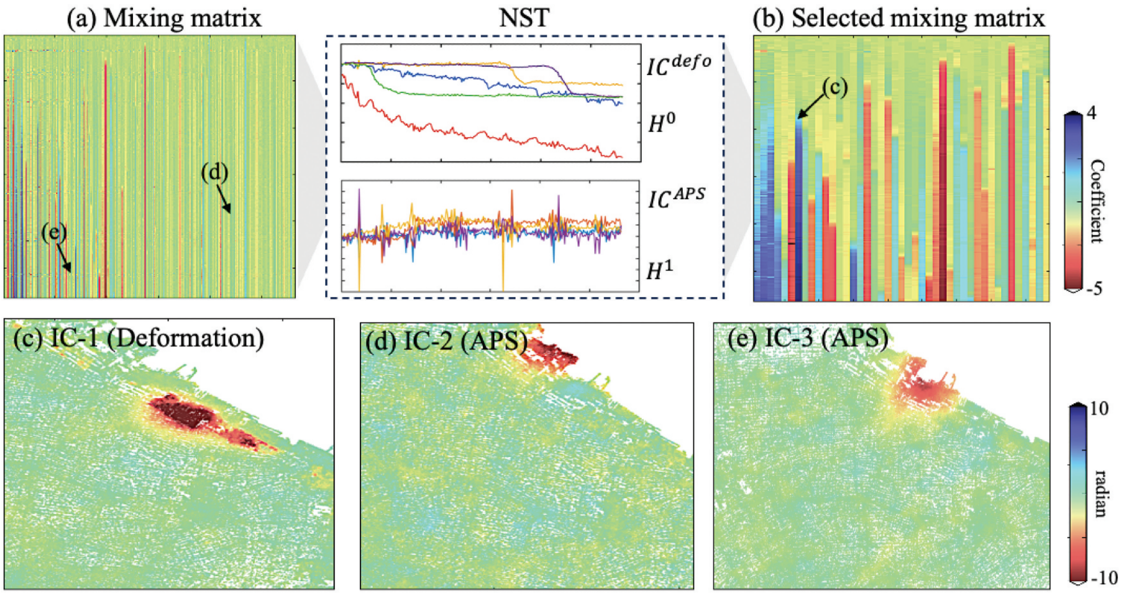

Figure 1. Example of non-stationarity test (NST) for selecting time-correlated columns from a mixing matrix, where each column represents the coefficient of a separated independent component over time. (a and b) Depict the original and selected mixing coefficient matrices, respectively. (c, d and e) Show the spatial patterns of three independent components related to deformation and APS effects, respectively.

SAR images used, denoted by N. The FastICA algorithm (Hyvarinen 1999) iteratively derives the mixing coefficient matrix ($\mathbf{A}$). Figure 1a presents an example of a mixing matrix, where each column represents the coefficient of an independent signal component. Figures 1c,d illustrate two examples of the spatial characteristics of independent components.

Given that the spatial distribution and timing of deformation are typically unknown a priori, it is difficult to identify the deformation signal based solely on the spatial characteristic among numerous separated independent components as shown in Figure 1. It is worth noting that deformation often occurs within a specific period and exhibits a smooth behavior. As demonstrated in Equation (6), we employed a single-master unwrapped IFG stack referred to the first acquisition date as the input for ICA, decomposing the data into a mixing matrix. In this matrix, each column will represent a time series. Columns that are associated with deformation will exhibit a discernible temporal trend. To automatically identify these deformation-related columns, we employ a statistical method known as the non-stationary test (NST). The test assesses whether observed temporal changes in a time series are consistent and indicative of non-stationary, as opposed to random fluctuations. Specifically, the Perron-Phillips unit root test is applied to each column of the mixing matrix to determine whether existing a unit root in the null hypothesis (H^0), indicating the non-stationary. The null hypothesis can be expressed as,

$$H^0 : x(t) = a \cdot x(t-1) + b \cdot t + c + e(t) \qquad (7)$$

where X(t) represent the value of the tested column of matrix ($\mathbf{A}$) at the t row; a is the autoregressive coefficient and $|a| = 1$ in H^0; b deterministic trend coefficient. c is the drift coefficient; $e(t)$ is a white noise error term. To carry out the test, we estimate the regression mentioned above and utilize standard t-statistics to assess the null hypothesis against the alternative hypothesis (H^1) that suggest stationary (absence of unit roots). The alternative hypothesis test can be expressed as,

$$H^1 : x(t) = a \cdot x(t-1) + b \cdot t + c + e(t) \qquad (8)$$

where $|a| < 1$. If the null hypothesis is accepted with a confidence level of 95%, the data series is suggested to have a unit root, suggesting the time series contains a time-related trend, a key indicator of deformation. It worth to note that some other iterative test methods can also be used for the non-stationary testing. Figure 1 illustrates the procedure of NST for identifying deformation-correlated components. Following the test on each column of the mixing matrix, all independent deformation components can be identified and used to form a so-called selected mixing matrix ($\widetilde{\mathbf{A}}$), as shown in Figure 1b, for reconstructing the deformation phase component ($\widetilde{\varphi}_{defo}$) together with the corresponding independent source vectors ($\widetilde{\mathbf{S}}$). The deformation phase is then reconstructed by,

$$\widetilde{\varphi}_{defo} = \widetilde{\mathbf{A}} * \widetilde{\mathbf{S}} \qquad (9)$$

When investigating ground deformation over a large area, the spatial pattern of deformation may be less prominent than the effects of the APS. In this case, a block-wise strategy can be implemented by segmenting the IFGs into smaller blocks. After separating signals in each block using the proposed method, the results from the blocks can be combined to reconstruct the complete deformation phase component.

2.3. Retrieval of deformation times series

Once the deformation phase components have been reconstructed, the deformation time series can be estimated using the standard MT-InSAR procedures,

$$\widetilde{\varphi}_{defo} = \kappa d^j, j = 1, 2, 3, \ldots .N$$
$$\widetilde{\mathbf{v}} = \text{minmize} \sum \left(d^j - \widetilde{\mathbf{v}} t^j\right)^2$$

with

$$\kappa = \frac{4\pi}{\lambda} \tag{10}$$

where κ represents the conversion ratio between the phase and deformation value; t^j is the time of (j)-th SAR acquisition relative to the first acquisition; d^j denotes the corresponding accumulated deformation; and λ is the radar wavelength. In short, the proposed approach enables automatic separation of APS and deformation signals in MT-InSAR, eliminating the necessity of manual intervention. The data processing workflow is illustrated in Figure 2.

3. Experiment with simulated data

To assess the effectiveness of the proposed method, we conducted experiments with simulated data for 1000 times, each using the same spatial deformation pattern but varying in time to simulate linear, abrupt, construction, and random deformation. In total, we simulated 70 SAR images within a two-year period, according to the parameters of the Sentinel-1 dataset. The APS was simulated using numerical functions (Kampes 2005), with maximum phase delays ranging from 5 to 12 rad across the simulations. Decorrelation noise was randomly added. The simulated phase components were linearly combined to form SAR images. A total of 233 IFGs were generated from the SAR images according to the interferometric pairs, as shown in Figure S1. The spatiotemporal baseline can be found in the supplementary material. We assumed that no phase components related to the topography and satellite orbits existed, and the IFGs were correctly unwrapped. Figures 3b,c present two examples of the IFGs, highlighting the varying APS effects.

To demonstrate the improvement with the use of the proposed method compared with the Kalman-based method and traditional small baseline subset (SBAS), we processed each simulated dataset using these three methods. A comparison of the results is displayed in Figures 3,4. The proposed method retrieved the spatial deformation pattern, which closely matched the simulated "real" deformation, as shown in Figure 3a,d. However, the deformation retrieved by the Kalman-based method and traditional SBAS still suffers from APS disturbance, as shown in Figure 3e, frespectively. Looking into the details of the deformation time series, some selected points are displayed in Figures 4a–d, representing the different temporal deformation types. Among them, the deformation time series estimated by the proposed method tend to be better solved than those estimated by the Kalman-based method and the traditional SBAS, particularly in identifying the turning point of the time series. The error statistics are further analyzed in Figures 4e–h, where the root-mean-square-error (RMSE) of the proposed method is lower than those of the other two methods. The RMSE of the proposed method is below 0.5 mm, whereas the RMSE of the traditional methods reach up to 3.28 mm.

To demonstrate the effectiveness of proposed method in APS mitigation, Figure 5 illustrates three

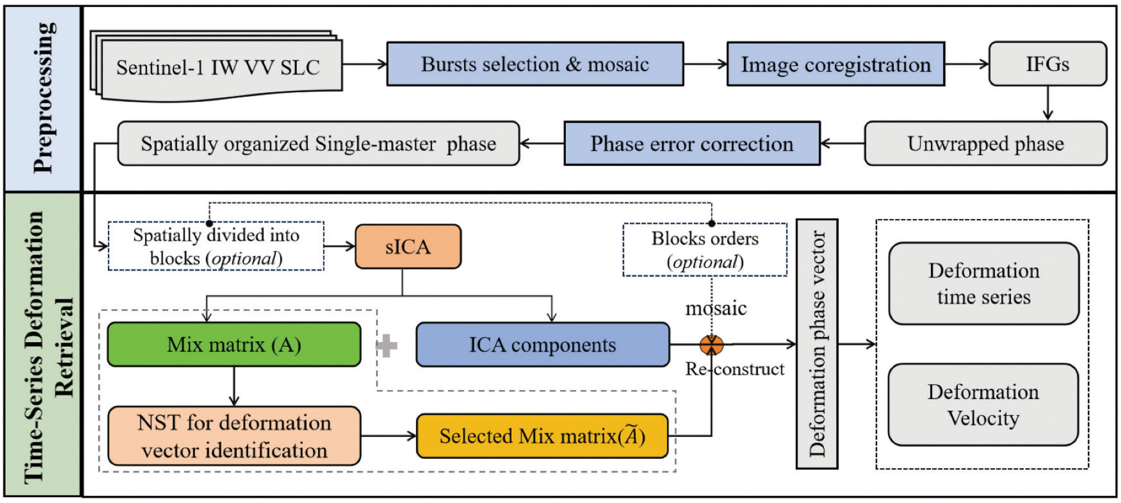

Figure 2. Flow chart of the proposed method.

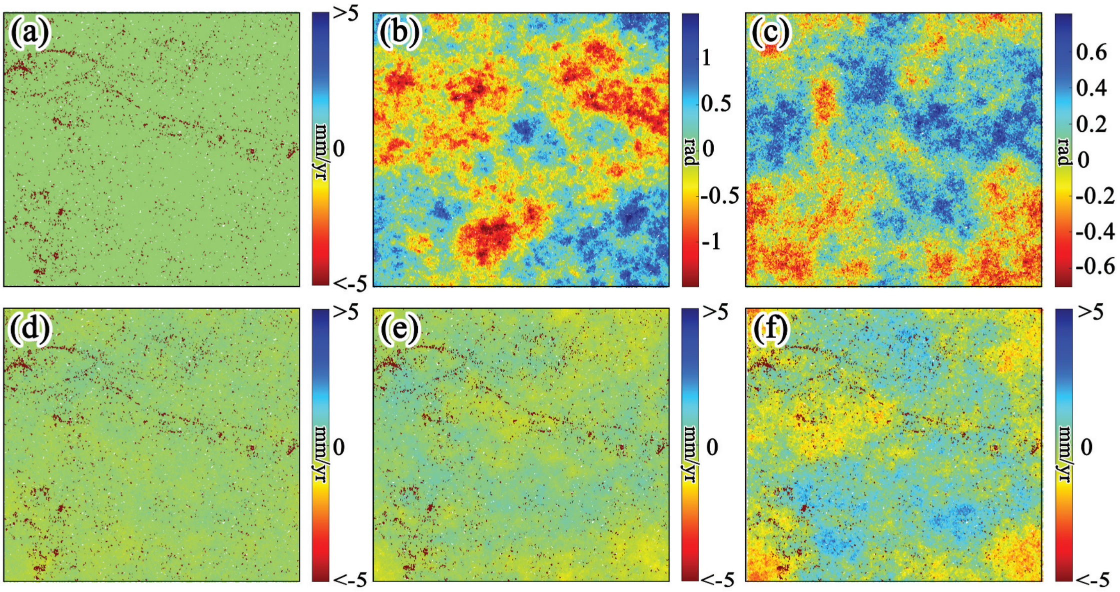

Figure 3. Examples of simulated IFGs. (a) Deformation velocity map; (b) and (c) IFGs affected by APS; (d–f) deformation velocity maps estimated by the proposed method, Kalman-based method and SBAS, respectively.

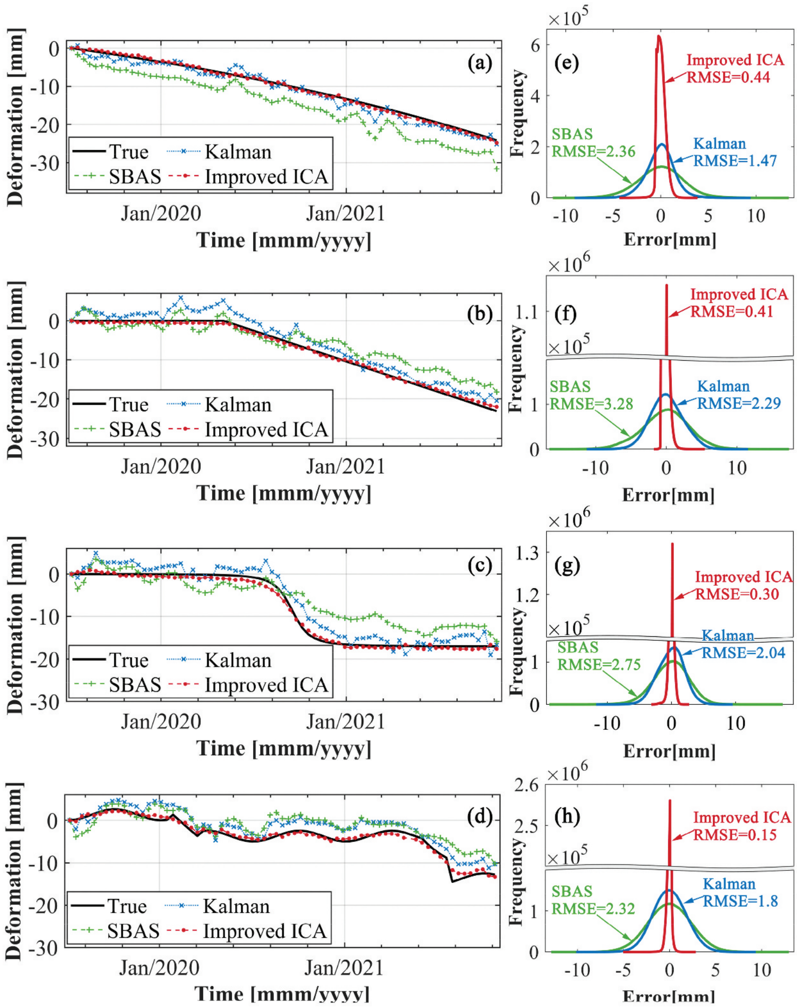

Figure 4. Comparison of the deformation time series on the selected points using different methods:(a–d) are the time series of four types of deformations;(e–h) show the histograms of the RMSEs corresponding to the simulated “real” value.

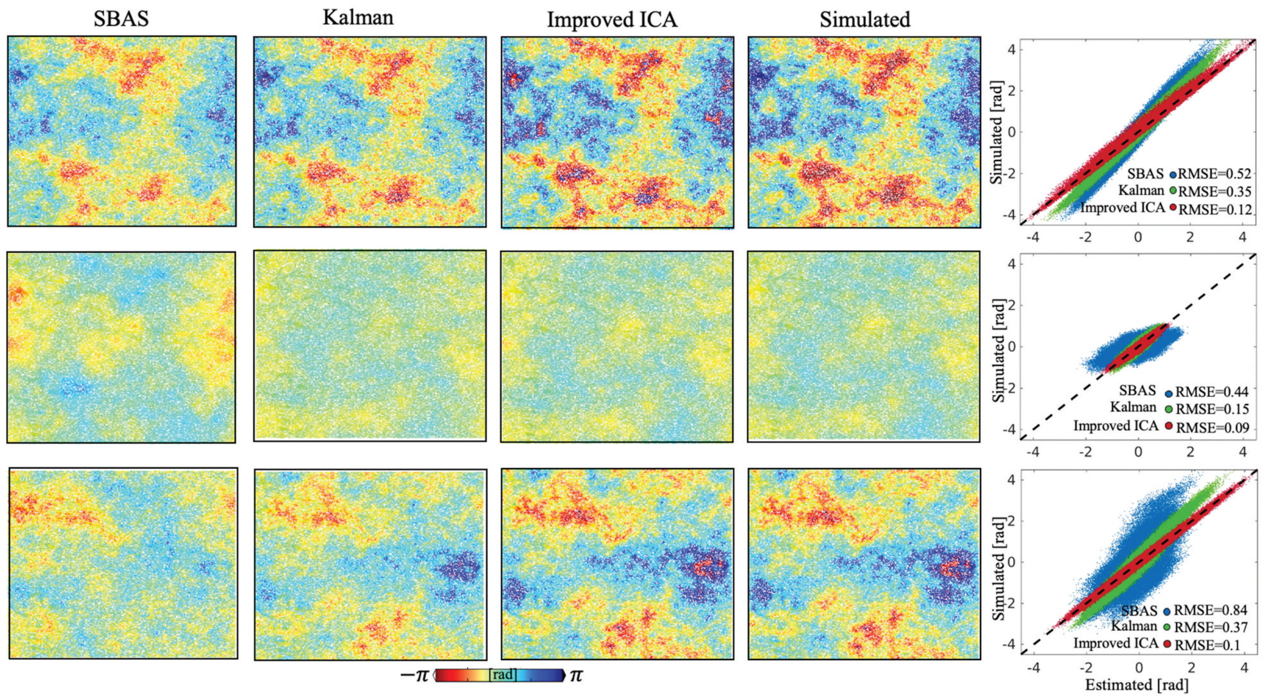

Figure 5. The comparison results of estimated APS with three different methods. The black dashed line in scatter plots represent the prefect alignment with simulated "real" APS phase.

examples of separated APS using different methods. The results suggest that the three methods achieved similar spatial patterns of the APS component, with the main differences distributed across some localized areas. The scatter plots in Figure 5 indicate that the proposed method aligns most closely with the simulated "real" APS effect, obtaining the lowest RMSE among the methods tested. In contrast, the traditional methods exhibit the significant differences in APS estimates, with a maximum RMSE of approximately 0.8 radians, which is higher than the 0.12 radian RMSE of the proposed method. The substantial difference highlights the accuracy improvement of the proposed method in both estimating and correcting the APS effect for MT-InSAR deformation monitoring. Furthermore, Figure 6 provides statistical information from the 1000 experiments, including the mean and standard deviation (STD) of RMSE for each method. The proposed method demonstrates significant advancements in ground deformation monitoring by achieving an average accuracy improvement of 50% across a range of deformation scenarios.

4. Experiment with real SAR data

4.1. Study area

The Nantong region, located in the northern coastal area of the Yangtze River estuary, China (Figure 7), has been selected as the experimental site to assess the performance of the proposed method. The region is characterized by an annual precipitation range of 1000–1200 mm, which presents challenges for InSAR deformation monitoring due to atmospheric

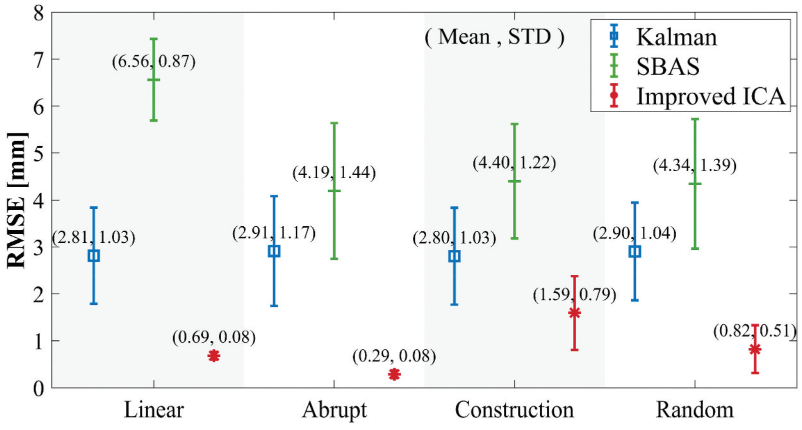

Figure 6. Statistical results of the RMSE obtained from 1000 simulation experiments for four types of temporal deformation.

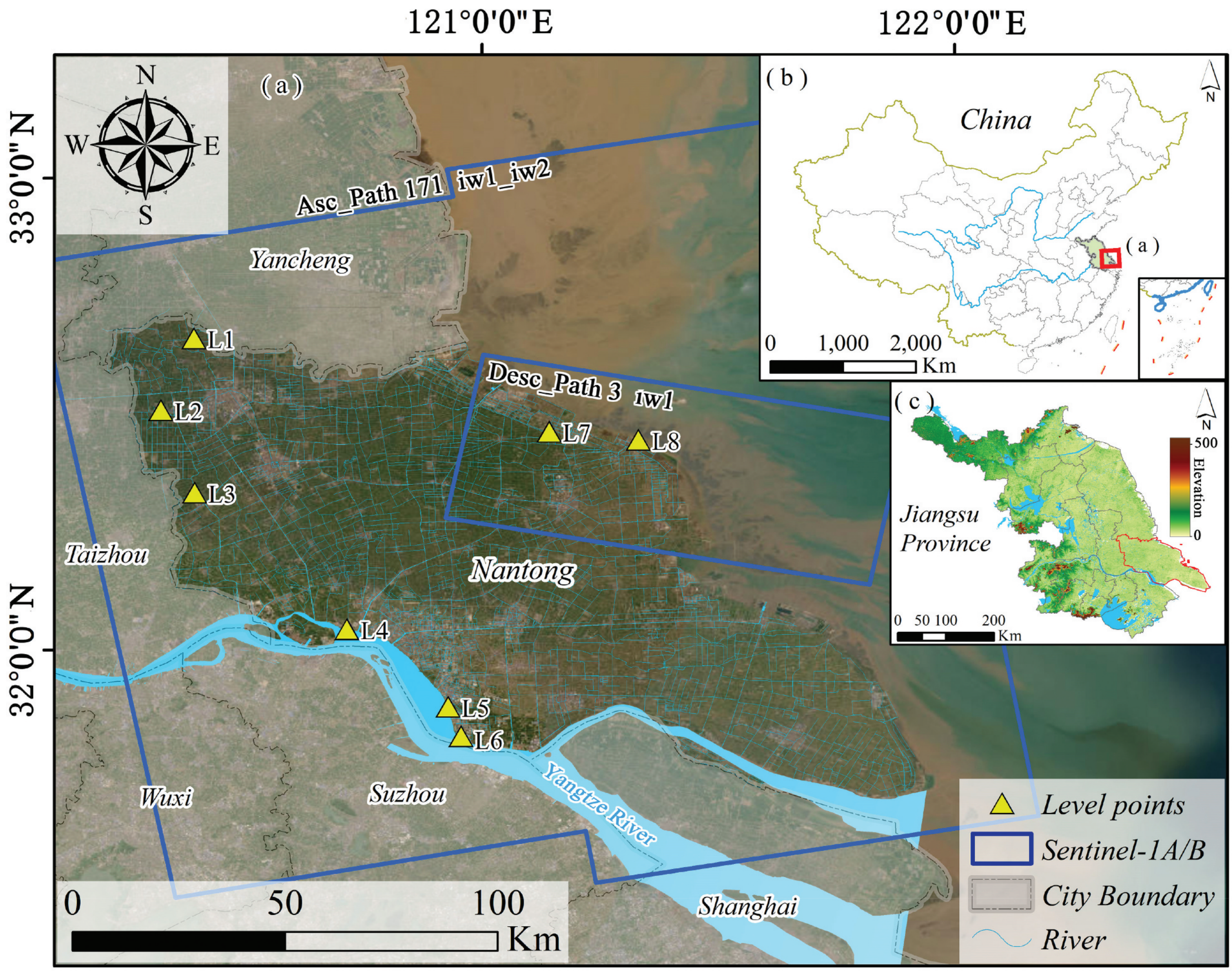

Figure 7. The study area and the data coverage. The blue rectangular are the coverage of the Sentinel-1 SAR data. The yellow triangles are the leveling stations that used for the InSAR results validation.

perturbations. In recent years, Nantong was experiencing rapid urbanization, including multiple civil constructions, such as transportation projects, underground developments, and land reservations (Zhang et al. 2021; Zhao et al. 2023). The geological composition is dominated by extensive quaternary sediments, with highly compressible soft soils that are susceptible to uneven ground deformation due to frequent construction activities (Zhan et al. 2022; Zhang et al. 2021). In addition, the high demand for water in industry and agriculture has resulted in considerable ground subsidence in many areas, predominantly along the coastal areas (Fan, Wang, and Li 2020), which will be discussed in Section 5.

4.2. Datasets

A total of 287 Sentinel-1 SAR satellite images was obtained from the European Space Agency (ESA) to investigate the ground deformation over the Nantong region. Among them, 283 were from the ascending orbital direction with a revisit time of 6 to 12 days from 26 February 2015, to 27 May 2023, and 4 were from the descending orbital direction during the period from 26 July 2016, to 24 October 2016. The spatial coverage of the achieved SAR datasets is illustrated in Figure 7, which marked with blue rectangles. Image information can be found in Table-S1 of the Supplementary Material. The Copernicus GLO-30 DSM (COP-DSM) (Fahrland 2020) with 1 arc second resolution and 4 m elevation accuracy, was used to simulate and compensate for the topographic phase during the InSAR data processing. In addition, ground subsidence measurements at eight benchmark leveling stations provided by the local government agency and adhere to the standards of second order leveling, were collected to validate the InSAR deformation results. The locations of these leveling stations are indicated by yellow triangles in Figure 7. Optical images sourced from Google Maps are used as the background to display the results and illustrate the various stages of construction.

4.3. Data processing

All the achieved SAR datasets were pre-processed with the GAMMA software (Wegnüller et al. 2016), including the image extraction, Sentinel burst selection,

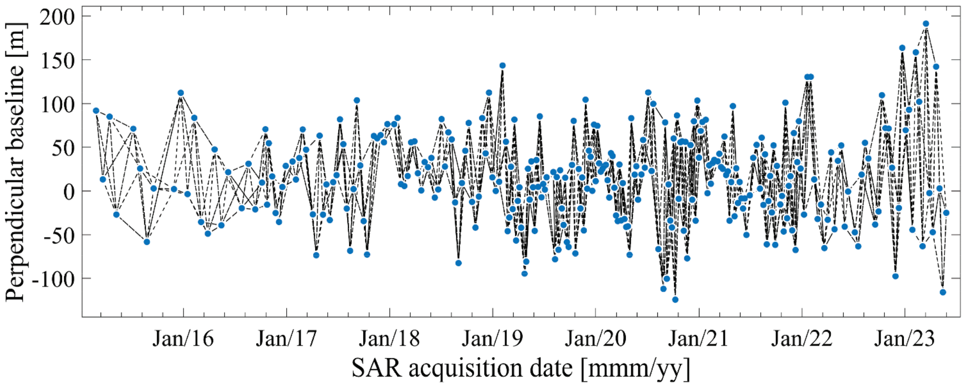

Figure 8. Spatiotemporal baseline network for data processing.

image coregistration, etc. A total of 843 IFGs were generated with a baseline threshold of 230 m and 100 days, as shown in Figure 8. The flat-earth phase and topographic phase were compensated for using Precise Orbit data and COP-DSM. Then, the unwrapped phase for each IFG was retrieved using the established methods (Wu et al. 2022). Corrections for orbital and topographic errors were applied using the methods described in (Liang et al., 2019b; Zhang et al. 2014). Following the workflow outlined in Figure 2, the deformation time series of selected coherent points was retrieved using the proposed method. For the purposes of comparison, both the traditional SBAS and the Kalman-based method were also applied to the same unwrapped dataset to retrieve the deformation results.

4.4. Results

Figure 9 illustrates some examples of the separation of APS and deformation phase components during the data processing over the Nantong region. The first row presents examples of identified independent patterns that varied along with the time, which can be recognized as the deformation phase. The subsequent rows display the separated APS phase components obtained using the proposed method, the SBAS method, and the Kalman-based method. The APS phases retrieved by all methods demonstrate similar spatial characteristics when compared to the original IFGs shown in the last row. However, the amplitude of the APS obtained through the conventional SBAS, and the Kalman-based methods is larger than that in the original IFG. The discrepancy is attributed to biased parameters in the regression modeling due to atmospheric effects, as indicated by the black square area in the lower right corner. In contrast, the amplitude of the APS retrieved by the proposed method aligns more closely with that in the original IFG. Furthermore, a noticeable deformation signal has remained in the APS component as identified by the traditional method, which is marked by the black dotted rectangular area. This issue mainly arises from the bias in deformation parameter estimation, which is affected by APS effects during the estimation process. In contrast, the proposed method effectively separates the APS and deformation components and is not susceptible to this factor.

Figure 10 presents the deformation velocity map of the Nantong region in the line-of-sight (LOS) direction, derived form ascending Sentinel-1 data from 26 February 2015, to 27 May 2023, using the proposed method. Negative values indicate deformation away from the satellite along the LOS direction (termed subsidence), while positive values indicate deformation toward the satellite along the LOS direction (termed uplift). The majority of the Nantong area appears stable with deformation rates predominantly between −15.0 mm/year and 15.0 mm/year, covering 97.2% of the measured deformation. Significant localized deformation is observed in the coastal zone, with rates ranging from −56.3 mm/year to 45.9 mm/year, as highlighted in Figure 10 (I, II, III, and IV). The largest subsidence area is highly correlated with the groundwater extraction, which will be discussed in Section 5.4. Urban areas, particularly those under development or renewal, are characterized by concentrated deformation patterns, as detailed in sections V, VI, VII, and VIII of Figure 10. The distinct deformation patterns are indicative of multi-source deformation mechanisms associated with urbanization, transportation infrastructure development, excessive groundwater use, and land reclamation projects, marked as A, B, C, D, and E on the map. The broader implications of these deformation patterns, such as their potential impact on urban infrastructure and land management strategies, will be further explored in Section 5.

5. Discussion

In this section, we conduct a comparative analysis of the proposed method and discuss the multiple types of ground deformation and their causal factors over the Nantong region.

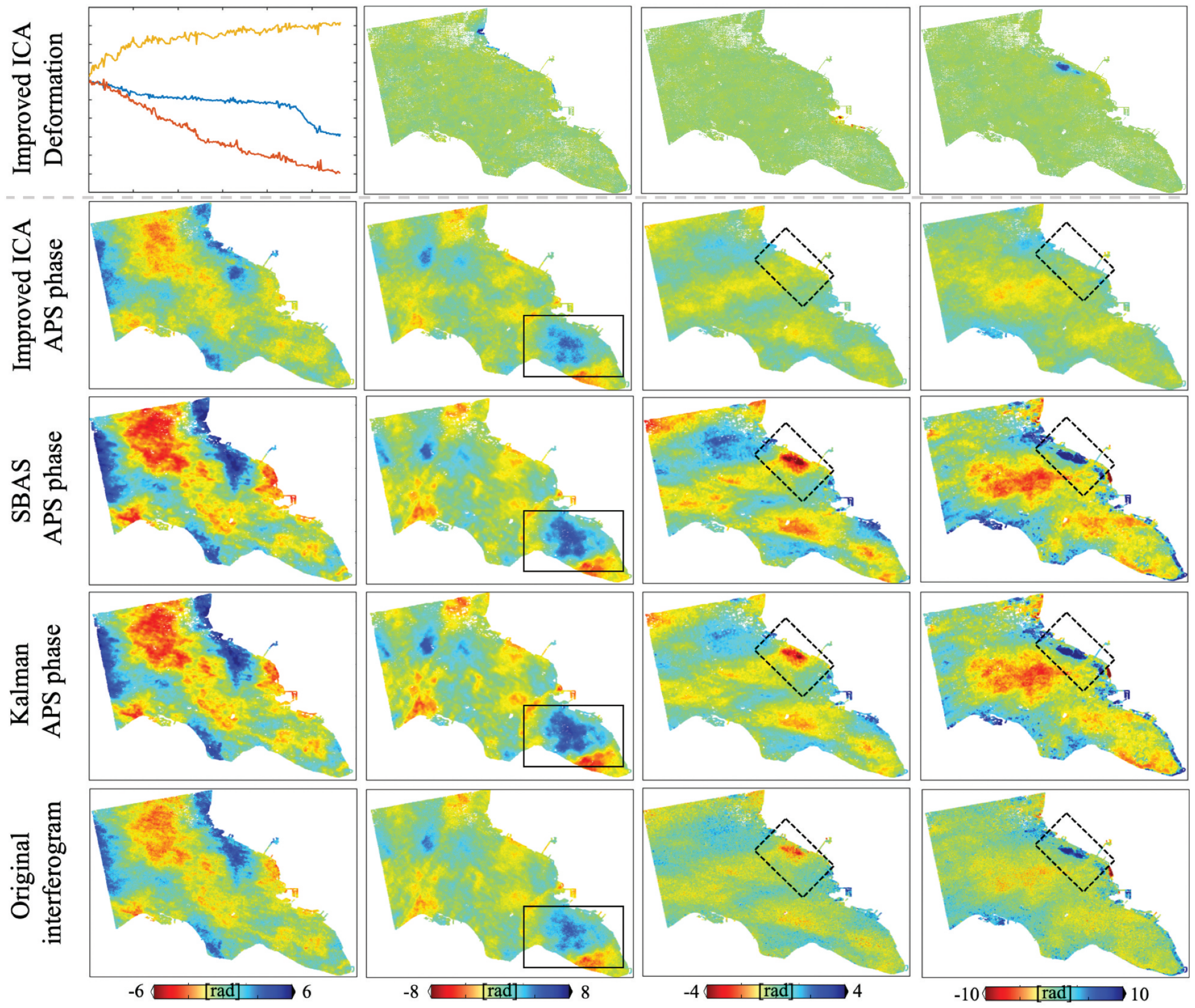

Figure 9. Examples of the separated phase component by three methods. First row is some examples of separated deformation component. Second, third and fourth rows are the separated APS phase component by the improved ICA method and the traditional methods, respectively. The last row is the corresponding original IFGs.

5.1. Accuracy assessment of the deformation measurements

To compare the performance of the proposed method and the traditional methods, we validated the InSAR-derived deformation using ground leveling measurements. Ground deformation from leveling stations was first converted to the LOS direction of InSAR according to the Sentinel-1 geometry using Equation (11).

$$d_{los} = d_{ver} \cos\theta \qquad (11)$$

where d_{los} is the deformation in the LOS direction; d_{ver} is the vertical deformation; θ is the satellite incidence angle.

We calculated the mean of all InSAR measurements within 100-m radius of the leveling stations. This radius was chosen to capture relevant spatial variability, ensuring that sufficient surrounding data were included to reflect local deformation patterns. We then compared mean values with the LOS deformation measured by leveling. Since leveling was conducted biennially from July 2016 to 2022, so the comparison was focused on this corresponding period by using the first leveling date as the zero reference. The comparison results are illustrated in Figure 11. Overall, the deformation time series estimated by the proposed method demonstrated higher reliability than those derived from traditional methods. For most stations, the InSAR-derived deformation showed high consistency with the leveling measurements. The proposed method achieved the highest accuracy, with an STD of less than 5.6 mm compared to the leveling measurements. The maximum error was less than 12 mm. In contrast, the STD for the traditional methods reached up to 15.4 mm, the maximum error reached up to 38 mm. The significant deviation between the leveling data and traditional methods, such as at L1, L2, and L4, was primarily attributed to inadequate mitigation of the APS effect, resulting in consistent biases and significant variation in the deformation time series.

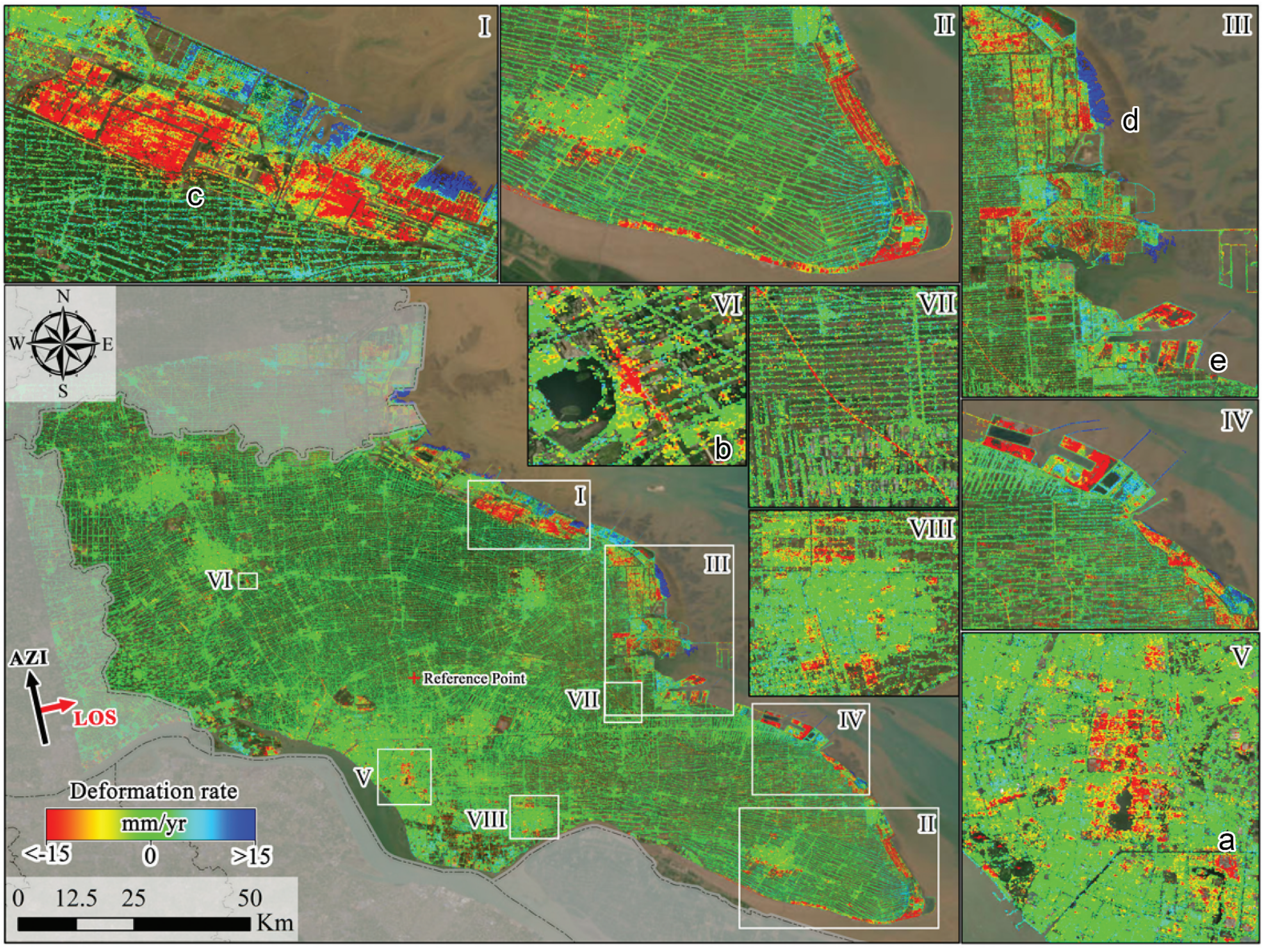

Figure 10. LOS ground deformation velocity map of Nantong from February 2015 to May 2023. To better display the deformation pattern, the color range is limited to −15 mm/yr and 15 mm/yr. Negative values indicate deformation away from the satellite along the LOS direction (termed subsidence), while positive values indicate deformation toward the satellite along the LOS direction (termed uplift). Subplots I–IV indicate significant localized deformation in the coastal zone related to groundwater extraction and land reservation projects, subplots V–VIII present deformation associated with urbanization efforts. Additionally, the five zones that represent typical deformation characteristics in Nantong (labeled a–e) are addressed in Section 5.1–5.5.

5.2. *Impact of the APS on the estimated deformation*

To assess the spatial impact of the APS effect on the InSAR-derived deformation map, we compared the cumulated deformation results over the past eight years obtained by both the traditional method and the proposed method, as illustrated in Figure 12. Visual inspection indicates that traditional methods are significantly affected by the APS effect, which may bias the velocity regression during the temporal detrending process and introduces consistent deviations across the accumulated deformation, particularly in the southeastern region of Nantong (see Figure 12a, b). Figure 9 also visualizes the areas affected by APS. In contrast, the deformation estimated by the proposed method, as shown in Figure 12c, achieved more convincing results, as indicated by the leveling measurements. The spatially coherent deformation pattern observed may reflect the effectiveness of our approach in mitigating the APS effect, which could enhance the validation of ground data. Such accuracy is essential for accurately identifying deformation distributions and assessing potential hazards.

Figure 13 illustrates a detailed comparison of the temporal APS effect on the deformation retrieval methods employed. Figures 13d,e present the deformation time series of two selected points, P1 and P2, within the construction area marked as zone A in Figure 10. Both points experienced notable ground deformation during the construction phase, with maximum cumulated LOS deformations exceeding −55 mm. Specifically, the ground was relatively stable during the pre-construction period, as shown in Figure 13a. Significant deformation began at the onset of the construction in January 2017. After the construction concluded in January 2020, the ground deformation trends decelerated and then stabilized, as shown in Figure 13c. This deformation evolution reflects a strong correlation with the construction stages. While all

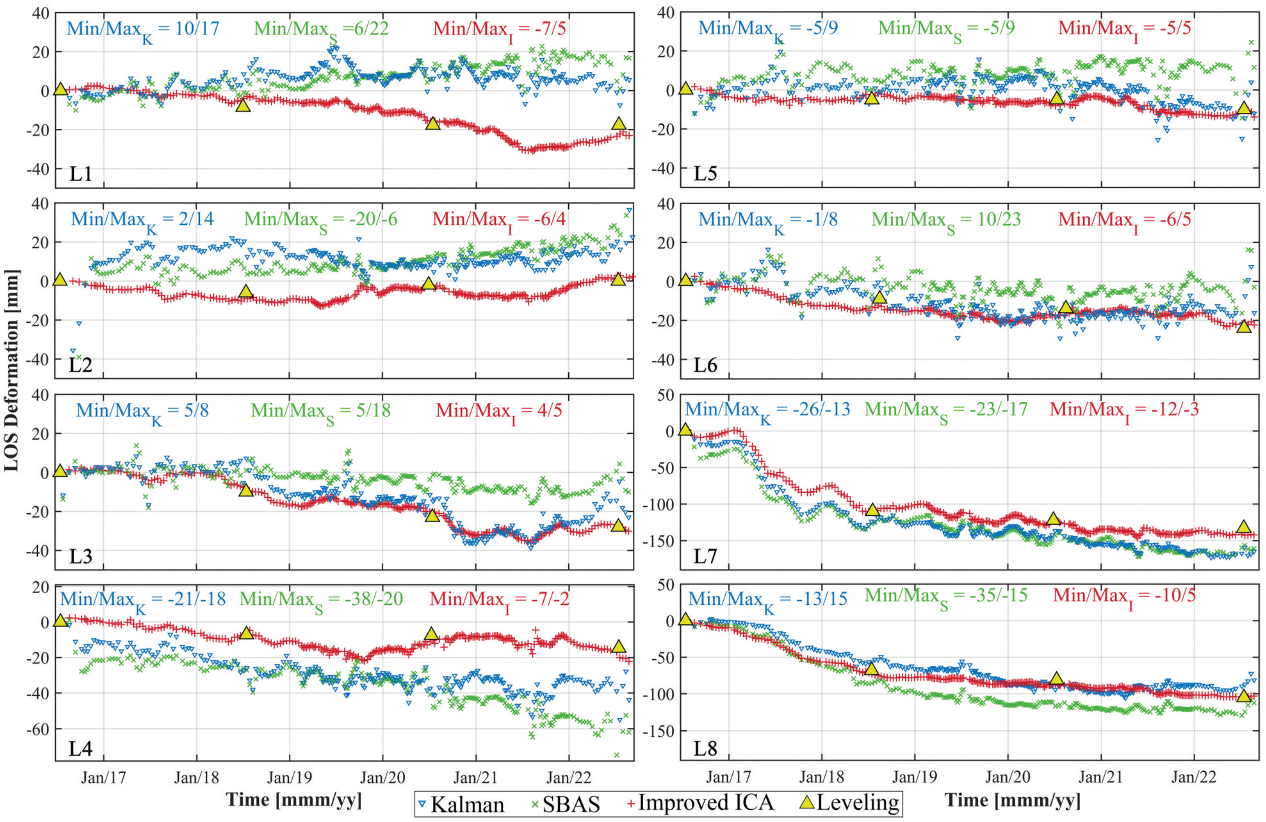

Figure 11. Comparison of InSAR-derived deformations (in the LOS direction) with leveling measurements for eight stations labeled L1 to L8. The minimum and maximum differences between them are indicated at the top of the figure. The unit is millimeters.

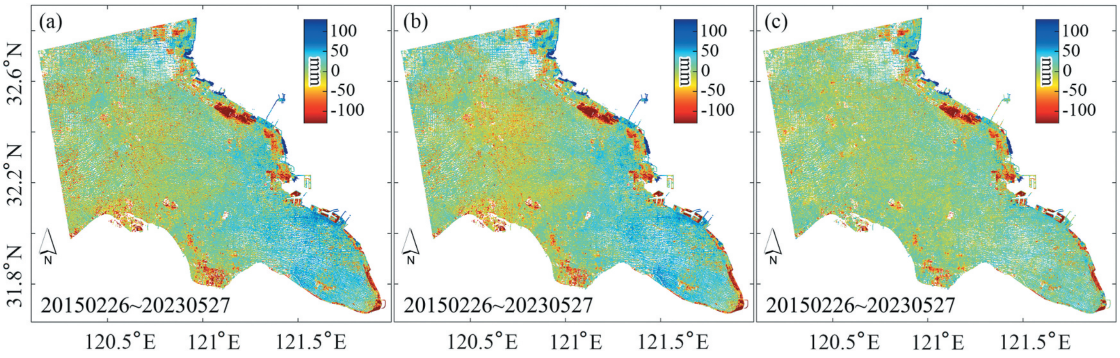

Figure 12. Cumulated deformation estimated using Sentinel-1 and the following methods: (a) Kalman-based method, (b) SBAS, and (c) the proposed method.

methods captured the deformation variation between the construction stages (see the optical images), the proposed method demonstrates potential advantages in providing more temporally coherent time series and identifying deformation turning points more accurately. This may significantly enhance the reliability of early warning and detection of potential hazards. In contrast, traditional methods seem to face challenges in accurately capturing deformation sequences, exhibiting significant variation, especially during periods without construction activity, likely due to insufficient APS correction for complex spatiotemporal atmospheric disturbances.

5.3. Deformation related to transport infrastructure construction

As introduced in Section 4.1, Nantong is undergoing rapid urbanization, characterized by extensive building renovations and the development of transportation networks. The presence of highly compressible soft soil layers in the region makes it susceptible to ground deformation induced by construction loads, which can potentially affect the stability and operation of surrounding infrastructure (Ramirez et al. 2022; Wu et al. 2021; Zhang et al. 2023). Figure 14 presents the ground deformation affecting critical transportation networks, including the Yancheng-Nantong

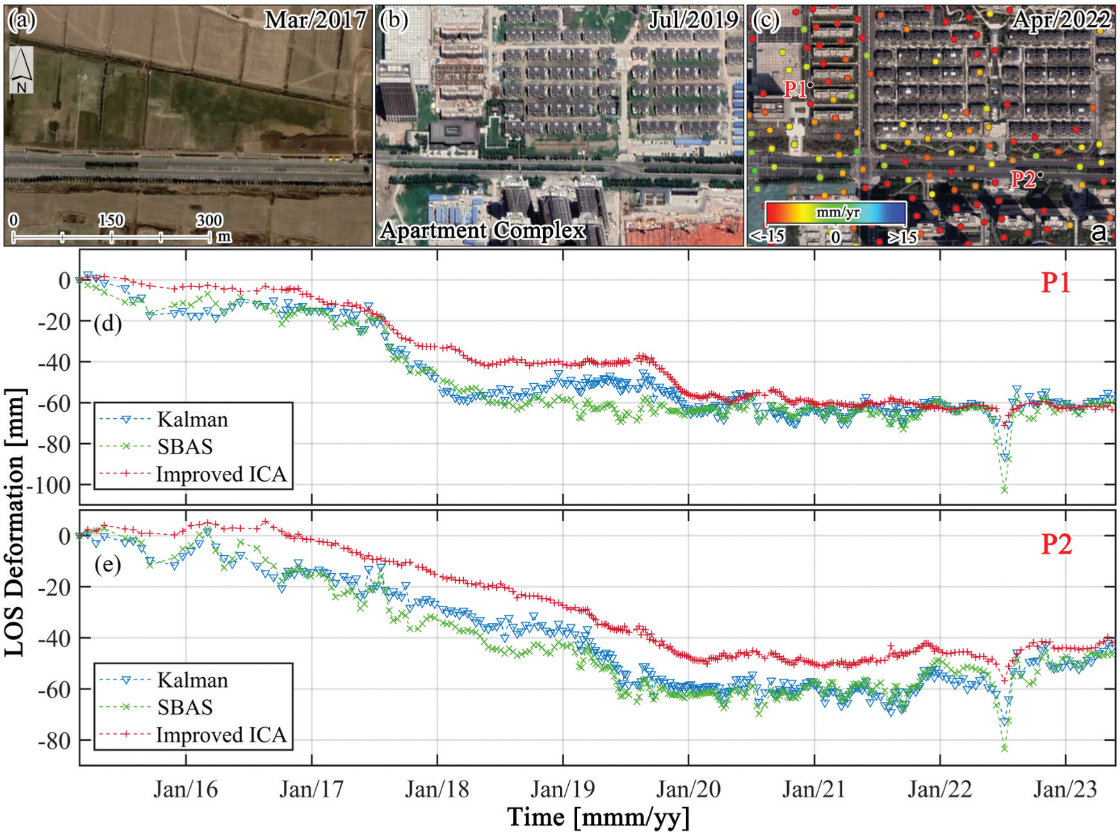

Figure 13. (a–c) Historical optical images of deformation zone a from different dates; (c) also overlays the deformation velocity. (d, e) compare the time series of two selected points shown in (c), estimated using Kalman-based, SBAS, and the proposed methods.

High-speed Railway (YNHR) project. The YNHR construction lasted from April 2018 to December 2020, during which InSAR results from the proposed method captured the deformation throughout this entire construction period, revealing approximately 150 mm of subsidence. The observed deformation closely aligned with the YNHR construction timeline, accurately capturing the progress of construction activities. According to the historical optical images and local practice report, the Rugao South Railway Station (RSRS), a component of the YNHR project, began construction in January 2020 and commenced operation concurrently with the YNHR. Consequently, the points P2–P4 were the first to experience significant deformation due to the construction activities, as they closest proximity to the railway. The deformation pattern observed at the monitoring point P1 is distinguished from that of the other selected points, which remained stable following the construction of the RSRS until February 2019.

5.4. Deformation related to ground water overdraft

The water supply of Nantong is primarily from the bedrock fissure water of the III confined aquifer and loose rock pore water (Li et al. 2019), which serve drinking, industrial production, agricultural irrigation, and other usages. However, decades of groundwater over-exploitation have led to a notable decline in groundwater levels and ground subsidence (Fan, Wang, and Li 2020; Zhan et al. 2022; Zhang et al. 2021). In this study, the significant deformation was also detected in the coastal area (Figures 10 and 15(a)). The maximum cumulative deformation exceeded −180 mm during the observation period from 2015 to 2023 (Figure 15(a)). Figure 15b,c indicate that this region is used for agriculture and has substantial aquaculture water demands (Zhan et al. 2022).

To explore the correlation between ground deformation and groundwater overdraft, we analyzed the deformation time series. Two points, P1 and P2, located in different areas of the deformation region, are selected for analysis, as shown in Figure 15d. Both points exhibit a consistent deformation pattern, although some variations occur over time. Additionally, seasonal patterns in time series of deformation, along with a decreasing trend in the rate of deformation, were observed. To further explore the characteristics of the deformation, the deformation trend was mitigated, and the residual values are shown in Figure 15e. The residual deformation indicates evident seasonal variations with an approximately one-year periodicity. To analyze the contributors to the periodic deformation, we collected

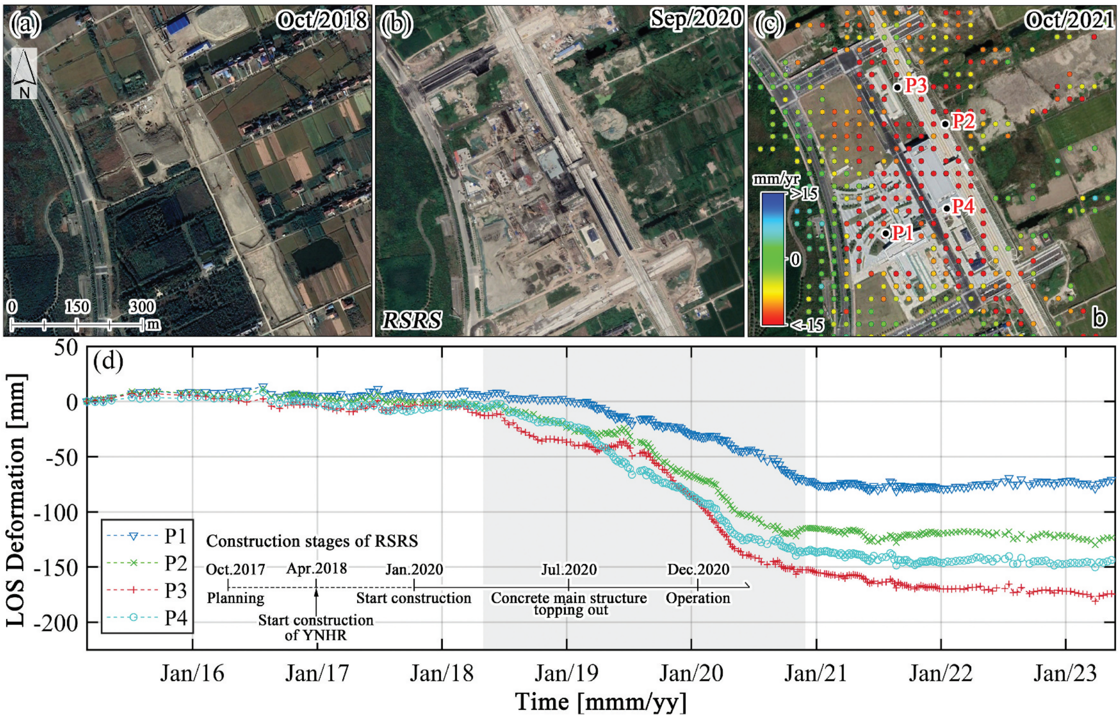

Figure 14. Ground deformation related to the transport infrastructure construction in zone B: (a–c) historical optical images (i.e. the Rugao South Railway Station, RSRS) from different dates; (c) also overlays the deformation velocity. (d) shows the time series of four selected points from (c), estimated using the proposed method.

monthly average precipitation data from the Nantong Water Resources Bulletin (Cao et al. 2023) for the years 2015 to 2022. The local rainy season occurs from July to August, as indicated by the gray shading in Figure 15e. Notably, the seasonal deformation observed from MT-InSAR and rainfall is inverted, suggesting that the periodic deformation is not related to rainfall. One potential explanation for this phenomenon is cyclical underground water usage. Zhang et al. (2021) also noted this recurring temporal pattern, linking it to the stages of laver cultivation. The laver harvest begins in December, which leads to significant groundwater extraction for cleaning until June or July. This results in a subsidence period with an estimated one-month lag between groundwater withdrawal and ground subsidence. After the harvest, the demand for groundwater for cleaning decreases, allowing the groundwater level to recover. Consequently, ground uplift is observed from September to January.

Furthermore, the local government implemented early intervention and adopted stringent measures in June 2021 to control groundwater use, including promotion of surface water use, a ban on new wells, reduced groundwater extraction, and gradually sealing of existing wells (Nantong Municipal People's Government 2021). As a result, the overall trend of subsidence and the amplitude of periodical deformation has significantly reduced, and the ground surface has become more stable after July 2021, marked by light blue in Figure 15d. Therefore, the deformation in this area is primarily attributed to the groundwater overdraft and the compaction of confined aquifer system, while periodic changes in ground deformation closely relate to seasonal water usage patterns, specifically groundwater changes. It is worth noting that the reduction in ground deformation in this region provides strong evidence of the effectiveness and positive impact of the local groundwater utilization policy measures.

5.5. Deformation related to coastal accretion and land reservation project

In this study, the research area, i.e. Nantong, is a coastal city with abundant mudflat resources reserved for urban land expansion (Xu et al. 2022). The SAR dataset with a 6-day revisit cycle is utilized, which is able to remain the interferometric phase coherent and detect the dynamic accretion of coastal tidal mudflats over time. This has been demonstrated in Figure 16c where the mean coherence matrix of all pixels over the mudflats area is shown (additional IFG examples can be found in Figure S3 and S4 in the Supplementary Material). The deformation results, shown in Figure 16d, indicate the mudflats primarily experienced uplift in the LOS direction. The monitored uplift can reach more than 300 mm during the observation period. To confirm this uplift signal, cross-validation was conducted using limited Sentinel-1 SAR data along descending orbit, which is presented in Figure S5 in the Supplementary Material.

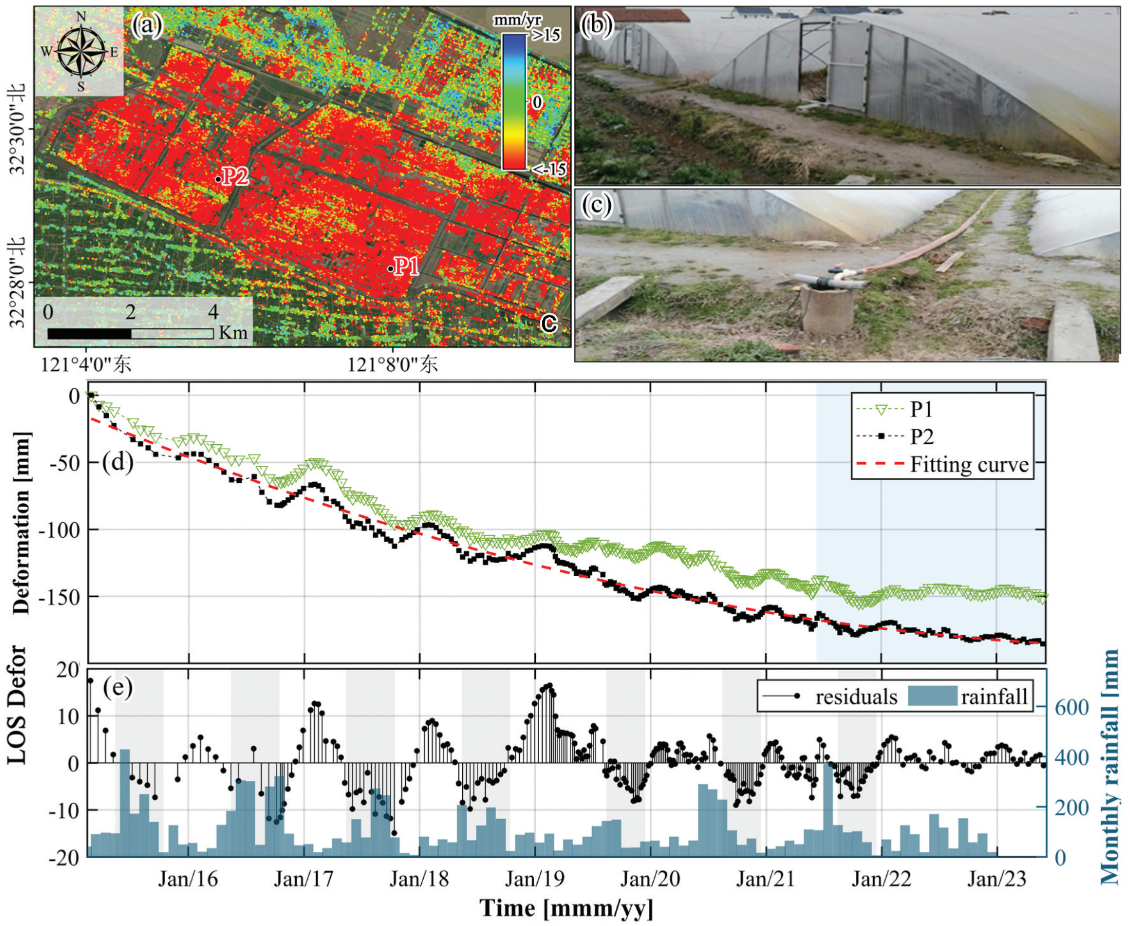

Figure 15. Ground deformation related to the groundwater overdraft in zone C: (a) LOS deformation velocity map; (b–c) two On-site photos of farming greenhouses and the well from (Zhan et al. 2022), which highlight the substantial groundwater demands. (d) the time series of two selected points from (a); (e) shows detrended time series of point P2 and monthly local precipitation.

Because the coastal area of the Nantong region is characterized by numerous river estuaries, abundant materials have been transported from upstream regions due to years of erosion. The observed uplift and deformation of the coastal mudflat can be primarily attributed to the accumulation of sediments delivered by the major rivers (Hulskamp et al. 2023; Ma et al. 2024; Murray et al. 2019). Variations in the spatial distribution of deformation across the tidal mudflats indicate differential sediment accumulation; the nearshore areas exhibit greater accumulation due to wave action, while the foreshore areas show less, likely due to reduced accretion from ongoing sediment deposition (Gao 2019). The temporal variation in deformation over the mudflats is captured through the time series of four selected points: P1 and P2 in the natural mudflat area, and P3 and P4 are located in the land reservation area (outlined by a white dashed box in Figures 16a,b). It can be seen that the monitoring points P1 and P2 demonstrate continuous uplift due to natural sediment accumulation, while points P3 and P4 exhibit subsidence after the completion of the dam for the land reservation project, which began in January 2019. The observed subsidence at P3 and P4 is likely a result of the disruption of sediment transport and the influence of wave action in the area, which has made the subsidence signal caused by soil consolidation more apparent.

Regarding subsidence related to the land reservation project, Figures 16f,g offer a more detailed perspective on the deformation occurring in the Tongzhou Bay area, where the reclamation activity had already finished before the observation period of the SAR data utilized in this study. The region experienced significant subsidence, reaching −350 mm in total, during the monitoring period. Therefore, building construction and soil self-compaction jointly cause significant ground subsidence in this area. Furthermore, it should be noted that multiple points (P5–P8) in different reclamation areas were selected for deformation time-series analysis, revealing that the construction processes in these areas did not occur simultaneously, but rather during different time periods. The proposed method successfully captured these deformation turning points, which can serve as valuable indicators for tracking the construction progress and offer references for future engineering projects.

5.6. Limitation and further work

Mitigating the APS effect in MT-InSAR deformation measurements is particularly challenging in coastal areas due to significant variations in water vapor. Traditional ICA-based methods often struggle to identify independent signal sources when prior

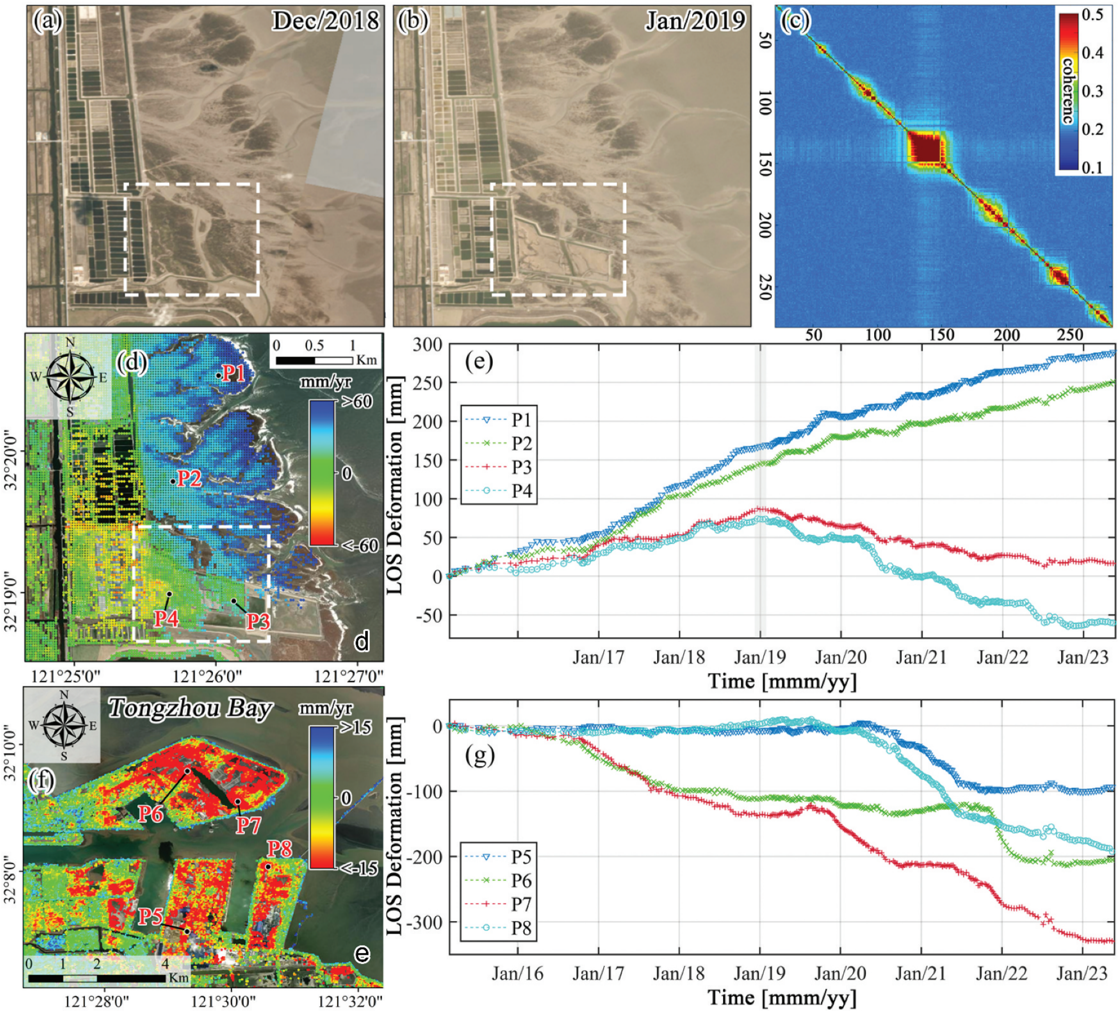

Figure 16. Ground deformation related to the coastal accretion and land reservation project in zones D and E: (a,b) historical optical images of zone D, (c) mean coherence matrix of all pixels over mudflat area in zone D, (d) the deformation velocity map of zone D, and (e) the time series of four selected points from (d). (f) The deformation velocity map of zone E, where the reclamation was completed before 2015; (g) the time series of four selected points from (f).

information is unavailable. The proposed method integrating the NST into procedure effectively addresses this issue by enabling automatic separation of deformation components and accurately capturing turning points in deformation time series. Because of the input data for the proposed method is the unwrapped IFG, which can be obtained through various methods. The proposed approach is independent of the MT-InSAR method and can be integrated with different methodologies. The case study in the Nantong area provides valuable insights into the spatiotemporal dynamics of ground deformation, enhancing our understanding of the relationship between land deformation and human activities. However, this study has some limitations. A notable drawback of the proposed method is its increased computational complexity and cost compared to traditional approaches, primarily due to the integration of ICA and NST procedures. Nonetheless, this added complexity is justified by the corresponding improvements in accuracy for deformation retrieval and turning point detection. Additionally, reliance on SAR data may restrict our analysis of spatial and temporal deformation characteristics in the Nantong area, particularly due to a lack of long-wavelength SAR images (e.g. L-band), which limits a more thorough investigation of tidal flat accretion e.g. the thick of the mudflats. For future studies, the proposed method could be adapted to a sequential ICA estimation procedure that eliminates the need to recalculate ICA components from the overall data to isolate the APS effect, significantly reducing computational costs. Moreover, based on the findings from the case studies, particularly those concerning tidal flat uplift and land reclamation projects, similar monitoring and analysis can be expanded to coastal areas worldwide to assess potential land resources for reclamation in tidal flats over the coming decades.

6. Conclusions

In this research, we propose an improved MT-InSAR method that effectively mitigate the effects of atmospheric phase screen (APS) in retrieving deformation time series. Our method employs an enhanced

Independent Component Analysis (ICA) to separate the APS from the deformation signals in each SAR interferogram (IFG). By implementing a non-stationary test to automatically identify and extract the deformation component derived from ICA, we account for the distinctive spatiotemporal characteristics of both deformation and APS. The experiment results demonstrate that the proposed method significantly improves the accuracy of the estimated deformation by an average of 50%, allowing for more precise identification of turning points between deformation trends. This improvement is particularly useful for identifying the correlation between deformation and construction activities. A case study in Nantong City, utilizing Sentinel-1 datasets from 2015 to 2023, reveals that our method achieved a standard deviation (STD) of 5.6 mm against leveling surveys, markedly better than the 15.4 mm STD observed with standard SBAS. The study indicates that the spatiotemporal evolution of deformation in Nantong is caused by multiple factors, i.e. construction activities, groundwater withdrawal, and land reservation project. Among which, groundwater extraction has been attributed to significant ground subsidence, which has decreased following the implementation of policies aimed at restricting groundwater usage. Our findings highlight a distinct accretion phenomenon along the Nantong coast, where the accretion area exhibits significant uplift that eventually shifts to subsidence, a change attributed to sediment accumulation and the implementation of land reclamation projects.

Disclosure statement

No potential conflict of interest was reported by the author(s).

Funding

This work is supported by the National Natural Science Foundation of China [Grant Nos. 42330717, 42304052], the University Grants Council of the Hong Kong Polytechnic University [Grant Nos. P0045896, P0050333, P0042898], the Research Grants Council of Hong Kong [Grant Nos. PolyU 152318/22E, PolyU 152344/23E, PolyU 152295/23E].

Notes on contributors

Zhijie Zhang is currently pursuing the M.S. degree in Photogrammetry and Remote Sensing with the School of Geology Engineering and Geomatics, Chang'an University, and working as a research assistant in the Department of Land Surveying and Geo-Informatics at The Hong Kong Polytechnic University, China. His research interests include multi-source remote sensing data processing, and the application of MT-InSAR for continuous monitoring of ground deformation.

Songbo Wu received the Ph.D. degree from The Hong Kong Polytechnic University in 2022. Currently, he is working as a Research Assistant Professor in the Department of Land Surveying and Geo-Informatics at The Hong Kong Polytechnic University, China. His research interests include data processing for multi-temporal InSAR, as well as applications related to urban civil infrastructure health monitoring and coastal geological hazards monitoring.

Guoqiang Shi received the Ph.D. degree in Earth System and Geoinformation Science from the Chinese University of Hong Kong (CUHK) in 2019. During 2018 and 2019, he was a visiting Ph.D. with the Department of Earth and Planetary Science, University of California Berkeley. From 2019 to 2022, he was a postdoc fellow with the Institute of Space and Earth Information Science, CUHK, China. He is currently an Assistant Professor with the Department of Land Surveying and Geo-Informatics, The Hong Kong Polytechnic University, China. His research interests include persistent/distributed scatterer interferometry and their applications to urban geo-hazards monitoring and modelling, built environment and infrastructure health diagnosis.

Xiaoli Ding received B.Eng. from Central South University of Metallurgy in 1983 and Ph.D. degree in geodesy from the University of Sydney, Sydney, NSW, Australia, in 1993. He is currently the Chair Professor of geomatics with the Department of Land Surveying and Geo-Informatics, and the Director with the Research Institution for Land and Space, The Hong Kong Polytechnic University, China. His individual research interests are in developing technologies for studying ground and structural deformation and geohazards.

Chaoying Zhao (Senior Member, IEEE) is currently a Professor with the School of Geology Engineering and Geomatics, Chang'an University. His research interests include SAR and InSAR techniques development and their applications.

Bochen Zhang is currently an Associate Professor with the College of Civil and Transportation Engineering, Shenzhen University, Shenzhen, China. His research interests include developing techniques for spaceborne and terrestrial radar interferometric data processing, with emphasis on geohazards and infrastructures' monitoring.

Liang Chen is with the Nantong Surveying and Mapping Research Institute Co., Ltd. His individual research interests focus on surveying and mapping ground information using innovative technologies for practical applications.

Zhong Lu is currently a Professor and the Endowed Shuler-Foscue Chair with the Roy M. Huffington Department of Earth Sciences, Southern Methodist University, Dallas, TX, USA. His research interests include the technique developments of InSAR processing and their applications to the study of volcano, landslide, and coastal processes.

ORCID

Zhijie Zhang http://orcid.org/0009-0004-5943-4257
Songbo Wu http://orcid.org/0000-0003-2118-0963
Guoqiang Shi http://orcid.org/0000-0001-6011-0269
Xiaoli Ding http://orcid.org/0000-0002-5733-3629
Chaoying Zhao http://orcid.org/0000-0002-5730-9602
Bochen Zhang http://orcid.org/0000-0002-2350-2084

Zhong Lu http://orcid.org/0000-0001-9181-1818

References

Bagheri-Gavkosh, M., S. M. Hosseini, B. Ataie-Ashtiani, Y. Sohani, H. Ebrahimian, F. Morovat, and S. Ashrafi. 2021. "Land Subsidence: A Global Challenge." *Science of the Total Environment* 778:146193. https://doi.org/10.1016/j.scitotenv.2021.146193.

Bekaert, D. P. S., A. Hooper, and T. J. Wright. 2015. "A Spatially Variable Power Law Tropospheric Correction Technique for InSAR Data." *Journal of Geophysical Research Solid Earth* 120 (2): 1345–1356. https://doi.org/10.1002/2014JB011558.

Berardino, P., G. Fornaro, R. Lanari, and E. Sansosti. 2002. "A New Algorithm for Surface Deformation Monitoring Based on Small Baseline Differential SAR Interferograms." *IEEE Transactions on Geoscience & Remote Sensing* 40 (11): 2375–2383. https://doi.org/10.1109/TGRS.2002.803792.

Cao, J. H., X. W. Jia, Z. Y. Huang, and L. Tian. 2023. "Nantong Water Resources Bulletin." Accessed January 1, 2024. http://www.nantong.gov.cn/ntsrmzf/gggs/content/91d7ec85-a0a5-4196-8f5f-e248f6999368.html.

Cao, Y. M., Z. W. Li, J. C. Wei, J. Hu, M. Duan, and G. C. Feng. 2018. "Stochastic Modeling for Time Series InSAR: With Emphasis on Atmospheric Effects." *Journal of Geodesy* 92 (2): 185–204. https://doi.org/10.1007/s00190-017-1055-5.

Chaussard, E., P. Milillo, R. Bürgmann, D. Perissin, E. J. Fielding, and B. Baker. 2017. "Remote Sensing of Ground Deformation for Monitoring Groundwater Management Practices: Application to the Santa Clara Valley During the 2012–2015 California Drought." *Journal of Geophysical Research Solid Earth* 122 (10): 8566–8582. https://doi.org/10.1002/2017JB014676.

Dinar, A., E. Esteban, E. Calvo, G. Herrera, P. Teatini, R. Tomás, Y. Li, P. Ezquerro, and J. Albiac. 2021. "We Lose Ground: Global Assessment of Land Subsidence Impact Extent." *Science of the Total Environment* 786:147415. https://doi.org/10.1016/j.scitotenv.2021.147415.

Ebmeier, S. K. 2016. "Application of Independent Component Analysis to Multitemporal InSAR Data with Volcanic Case Studies." *Journal of Geophysical Research Solid Earth* 121 (12): 8970–8986. https://doi.org/10.1002/2016JB013765.

ElGharbawi, T., and M. Tamura. 2014. "Measuring Deformations Using SAR Interferometry and GPS Observables with Geodetic Accuracy: Application to Tokyo, Japan." *ISPRS Journal of Photogrammetry & Remote Sensing* 88:156–165. https://doi.org/10.1016/j.isprsjprs.2013.12.005.

Fahrland, E. 2020. "Copernicus DEM Product Handbook (V3. 0)." *Airbus Def. Space GmbH Taufkirch. Ger* https://object.cloud.sdsc.edu/v1/AUTH_opentopography/www/metadata/Copernicus_metadata.pdf .

Falabella, F., A. Pepe, A. Perrone, and T. A. Stabile. 2024. "A Variance-Covariance Method to Estimating the Errors of 3-D Ground Displacement Time-Series Using Small Baseline InSAR Algorithms and Multi-Platform SAR Data." *ISPRS Journal of Photogrammetry & Remote Sensing* 211:208–227. https://doi.org/10.1016/j.isprsjprs.2024.04.006.

Fan, X. T., W. Wang, and M. M. Li. 2020. "Land Subsidence Detection of Nantong Area Based on Sentinel-1A TOPS by Using Time Series of InSAR Data." *Geomatics World (In Chinese)* 27 (5): 129–133+139. https://doi.org/10.3969/j.issn.1672-1586.2020.05.021.

Fattahi, H., and F. Amelung. 2013. "DEM Error Correction in InSAR Time Series." *IEEE Transactions on Geoscience & Remote Sensing* 51 (7): 4249–4259. https://doi.org/10.1109/TGRS.2012.2227761.

Ferretti, A., and C. Prati. 2000. "Nonlinear Subsidence Rate Estimation Using Permanent Scatterers in Differential SAR Interferometry." *IEEE Transactions on Geoscience & Remote Sensing* 38 (5): 2202–2212. https://doi.org/10.1109/36.868878.

Ferretti, A., C. Prati, and F. Rocca. 2001. "Permanent Scatterers in SAR Interferometry." *IEEE Transactions on Geoscience & Remote Sensing* 39 (1): 8–20. https://doi.org/10.1109/36.898661.

Gaddes, M. E., A. Hooper, and M. Bagnardi. 2019. "Using Machine Learning to Automatically Detect Volcanic Unrest in a Time Series of Interferograms." *Journal of Geophysical Research Solid Earth* 124 (11): 12304–12322. https://doi.org/10.1029/2019JB017519.

Gaddes, M. E., A. Hooper, M. Bagnardi, H. Inman, and F. Albino. 2018. "Blind Signal Separation Methods for InSAR: The Potential to Automatically Detect and Monitor Signals of Volcanic Deformation." *Journal of Geophysical Research Solid Earth* 123 (11): ,10,226–10,251. https://doi.org/10.1029/2018JB016210.

Gao, S. 2019. "Chapter 10 - Geomorphology and Sedimentology of Tidal Flats." In *Coastal Wetlands*, 2nd ed. 359–381. https://doi.org/10.1016/B978-0-444-63893-9.00010-1.

Hanssen, R. F. 2001. *Radar Interferometry: Data Interpretation and Error Analysis*. 2. Springer Science & Business Media. https://link.springer.com/book/10.1007/0-306-47633-9.

Herrera-García, G., P. Ezquerro, R. Tomás, M. Béjar-Pizarro, J. López-Vinielles, M. Rossi, R. M. Mateos, et al. 2021. "Mapping the Global Threat of Land Subsidence." *Science* 371 (6524): 34–36. https://doi.org/10.1126/science.abb8549.

Hou, J. X., B. Xu, J. Wei, Z. W. Li, Y. Zhu, W. X. Mao, and W. Z. Liu. 2024. "Noise Separation and Refinement for InSAR Deformation Time Series by Considering Sequence Non-Stationarity." *Chinese Journal of Geophysics (In Chinese)* 67 (11): 4077–4088. https://doi.org/10.6038/cjg2023R0266.

Huang, Q. H., M. Crosetto, O. Monserrat, and B. Crippa. 2017. "Displacement Monitoring and Modelling of a High-Speed Railway Bridge Using C-Band Sentinel-1 Data." *ISPRS Journal of Photogrammetry & Remote Sensing* 128:204–211. https://doi.org/10.1016/j.isprsjprs.2017.03.016.

Hulskamp, R., A. Luijendijk, B. van Maren, A. Moreno-Rodenas, F. Calkoen, E. Kras, S. Lhermitte, and S. Aarninkhof. 2023. "Global Distribution and Dynamics of Muddy Coasts." *Nature Communications* 14 (1): 8259. https://doi.org/10.1038/s41467-023-43819-6.

Hyvarinen, A. 1999. "Fast and Robust Fixed-Point Algorithms for Independent Component Analysis." *IEEE Transactions on Neural Networks* 10 (3): 626–634. https://doi.org/10.1109/72.761722.

Jung, J., D. J. Kim, and S. E. Park. 2014. "Correction of Atmospheric Phase Screen in Time Series InSAR Using WRF Model for Monitoring Volcanic Activities." *IEEE Transactions on Geoscience & Remote Sensing* 52 (5): 2678–2689. https://doi.org/10.1109/TGRS.2013.2264532.

Kampes, B. M. 2005. “Displacement Parameter Estimation Using Permanent Scatterer Interferometry” Ph. D. thesis, Dutch: Delft University of Technology. https://resolver.tudelft.nl/uuid:9f11f2ef-2db4-4583-a763-aee88e06ee3b.

Kim, J. W., Z. Lu, Y. Y. Jia, and C. K. Shum. 2015. “Ground Subsidence in Tucson, Arizona, Monitored by Time-Series Analysis Using Multi-Sensor InSAR Datasets from 1993 to 2011.” *ISPRS Journal of Photogrammetry & Remote Sensing* 107:126–141. https://doi.org/10.1016/j.isprsjprs.2015.03.013.

Kirui, P. K., E. Reinosch, N. Isya, B. Riedel, and M. Gerke. 2021. “Mitigation of Atmospheric Artefacts in Multi Temporal InSAR: A Review.” *Pfg-Journal of Photogrammetry Remote Sensing and Geoinformation Science* 89 (3): 251–272. https://doi.org/10.1007/s41064-021-00138-z.

Li, Z. H., E. J. Fielding, P. Cross, and J. P. Muller. 2006. “Interferometric Synthetic Aperture Radar Atmospheric Correction: GPS Topography-Dependent Turbulence Model.” *Journal of Geophysical Research Solid Earth* 111 (B2): 111 (B2. https://doi.org/10.1029/2005JB003711.

Li, Z., Z. J. Luo, Q. Wang, J. J. Du, W. Lu, and D. Ning. 2019. “A Three-Dimensional Fluid-Solid Model, Coupling High-Rise Building Load and Groundwater Abstraction, for Prediction of Regional Land Subsidence.” *Hydrogeology Journal* 27 (4): 1515–1526. https://doi.org/10.1007/s10040-018-01920-x.

Li, Z. W., X. L. Ding, and G. X. Liu. 2004. “Modeling Atmospheric Effects on InSAR with Meteorological and Continuous GPS Observations: Algorithms and Some Test Results.” *Journal of Atmospheric and Solar-Terrestrial Physics* 66 (11): 907–917. https://doi.org/10.1016/j.jastp.2004.02.006.

Liang, H. Y., L. Zhang, Z. Lu, and X. Li. 2019. “Nonparametric Estimation of DEM Error in Multitemporal InSAR.” *IEEE Transactions on Geoscience & Remote Sensing* 57 (12): 10004–10014. https://doi.org/10.1109/TGRS.2019.2930802.

Liang, H., L. Zhang, X. Ding, Z. Lu, and X. Li. 2019. “Toward Mitigating Stratified Tropospheric Delays in Multitemporal InSAR: A Quadtree Aided Joint Model.” *IEEE Transactions on Geoscience & Remote Sensing* 57 (1): 291–303. https://doi.org/10.1109/TGRS.2018.2853706.

Liao, M. S., H. J. Jiang, Y. Wang, T. Wang, and L. Zhang. 2013. “Improved Topographic Mapping Through High-Resolution SAR Interferometry with Atmospheric Effect Removal.” *ISPRS Journal of Photogrammetry & Remote Sensing* 80:72–79. https://doi.org/10.1016/j.isprsjprs.2013.03.008.

Ma, P. F., C. Yu, Z. Y. Jiao, Y. Zheng, Z. R. Wu, W. F. Mao, and H. Lin. 2024. “Improving Time-Series InSAR Deformation Estimation for City Clusters by Deep Learning-Based Atmospheric Delay Correction.” *Remote Sensing of Environment* 304:114004. https://doi.org/10.1016/j.rse.2024.114004.

Maubant, L., E. Pathier, S. Daout, M. Radiguet, M. P. Doin, E. Kazachkina, V. Kostoglodov, N. Cotte, and A. Walpersdorf. 2020. “Independent Component Analysis and Parametric Approach for Source Separation in InSAR Time Series at Regional Scale: Application to the 2017–2018 Slow Slip Event in Guerrero (Mexico).” *Journal of Geophysical Research Solid Earth* 125 (3): e2019JB018187. https://doi.org/10.1029/2019JB018187.

Murray, N. J., S. R. Phinn, M. DeWitt, R. Ferrari, R. Johnston, M. B. Lyons, N. Clinton, D. Thau, and R. A. Fuller. 2019. “The Global Distribution and Trajectory of Tidal Flats.” *Nature* 565 (7738): 222–225. https://doi.org/10.1038/s41586-018-0805-8.

Nantong Municipal People’s Government. 2021. “The Decision of the Municipal Government on Amending the “Nantong Groundwater Management Measures”.” June 10. https://www.nantong.gov.cn/ntsrmzf/yx/content/d87f9e41-1f3e-493d-87c7-a2ab396ff070.html.

Peng, M. M., Z. Lu, C. Y. Zhao, M. Motagh, L. Bai, B. D. Conway, and H. Y. Chen. 2022. “Mapping Land Subsidence and Aquifer System Properties of the Willcox Basin, Arizona, from InSAR Observations and Independent Component Analysis.” *Remote Sensing of Environment* 271:112894. https://doi.org/10.1016/j.rse.2022.112894.

Ramirez, R. A., G. J. Lee, S. K. Choi, T. H. Kwon, Y. C. Kim, H. H. Ryu, S. Y. Kim, B. Bae, and C. Hyun. 2022. “Monitoring of Construction-Induced Urban Ground Deformations Using Sentinel-1 PS-InSAR: The Case Study of Tunneling in Dangjin, Korea.” *International Journal of Applied Earth Observation and Geoinformation* 108:102721. https://doi.org/10.1016/j.jag.2022.102721.

Rigamonti, S., G. Dattola, P. Frattini, and G. B. Crosta. 2023. “A Multivariate Time Series Analysis of Ground Deformation Using Persistent Scatterer Interferometry.” *Remote Sensing* 15 (12): 3082. https://doi.org/10.3390/rs15123082.

Rouet-Leduc, B., R. Jolivet, M. Dalaison, P. A. Johnson, and C. Hulbert. 2021. “Autonomous Extraction of Millimeter-Scale Deformation in InSAR Time Series Using Deep Learning.” *Nature Communications* 12 (1): 6480. https://doi.org/10.1038/s41467-021-26254-3.

Schlögl, M., B. Widhalm, and M. Avian. 2021. “Comprehensive Time-Series Analysis of Bridge Deformation Using Differential Satellite Radar Interferometry Based on Sentinel-1.” *ISPRS Journal of Photogrammetry & Remote Sensing* 172:132–146. https://doi.org/10.1016/j.isprsjprs.2020.12.001.

Shi, G. Q., B. Huang, A. K. Leung, C. W. W. Ng, Z. L. Wu, and H. Lin. 2022. “Millimeter Slope Ratcheting from Multitemporal SAR Interferometry with a Correction of Coastal Tropospheric Delay: A Case Study in Hong Kong.” *Remote Sensing of Environment* 280:113148. https://doi.org/10.1016/j.rse.2022.113148.

Shirzaei, M., J. Freymueller, T. E. Törnqvist, D. L. Galloway, T. Dura, and P. S. J. Minderhoud. 2021. “Measuring, Modelling and Projecting Coastal Land Subsidence.” *Nature Reviews Earth and Environment* 2 (1): 40–58. https://doi.org/10.1038/s43017-020-00115-x.

Wegnüller, U., C. Werner, T. Strozzi, A. Wiesmann, O. Frey, and M. Santoro. 2016. “Sentinel-1 Support in the GAMMA Software.” *Procedia Computer Science* 100:1305–1312. https://doi.org/10.1016/j.procs.2016.09.246.

Wen, N. L., K. Dai, J. Deng, C. Liu, R. B. Liang, B. Yu, and W. K. Feng. 2024. “Periodic Displacement Accurate Extraction of Reservoir Active Slopes Through InSAR Observation and Independent Component Analysis-Based Wavelet Transform.” *International Journal of Applied Earth Observation and Geoinformation* 130:103919. https://doi.org/10.1016/j.jag.2024.103919.

Wu, S. B., B. C. Zhang, X. L. Ding, N. Shahzad, L. Zhang, and Z. Lu. 2022. “A Hybrid Method for MT-InSAR Phase

Unwrapping for Deformation Monitoring in Urban Areas." *International Journal of Applied Earth Observation and Geoinformation* 112:112. https://doi.org/10.1016/j.jag.2022.102963.

Wu, S. B., B. C. Zhang, H. Y. Liang, C. S. Wang, X. L. Ding, and L. Zhang. 2021. "Detecting the Deformation Anomalies Induced by Underground Construction Using Multiplatform MT-InSAR: A Case Study in to Kwa Wan Station, Hong Kong." *IEEE Journal of Selected Topics in Applied Earth Observations & Remote Sensing* 14:9803–9814. https://doi.org/10.1109/jstars.2021.3113672.

Xia, Z. G., M. Motagh, T. Li, M. M. Peng, and S. Roessner. 2023. "A Methodology to Characterize 4D Post-Failure Slope Instability Dynamics Using Remote Sensing Measurements: A Case Study of the Aniangzhai Landslide in Sichuan, Southwest China." *ISPRS Journal of Photogrammetry & Remote Sensing* 196:402–414. https://doi.org/10.1016/j.isprsjprs.2023.01.006.

Xia, Z. G., M. Motagh, W. D. Wang, T. Li, M. M. Peng, C. F. Zhou, and S. Karimzadeh. 2024. "Modeling Slope Instabilities with Multi-Temporal InSAR Considering Hydrogeological Triggering Factors: A Case Study Across Badong County in the Three Gorges Area." *Remote Sensing of Environment* 309:114212. https://doi.org/10.1016/j.rse.2024.114212.

Xu, N., Y. Q. Wang, C. H. Huang, S. Jiang, M. M. Jia, and Y. Ma. 2022. "Monitoring Coastal Reclamation Changes Across Jiangsu Province During 1984–2019 Using Landsat Data." *Marine Policy* 136:104887. https://doi.org/10.1016/j.marpol.2021.104887.

Xue, F. Y., X. L. Lv, F. J. Dou, and Y. Yun. 2020. "A Review of Time-Series Interferometric SAR Techniques: A Tutorial for Surface Deformation Analysis." *IEEE Geoscience and Remote Sensing Magazine* 8 (1): 22–42. https://doi.org/10.1109/MGRS.2019.2956165.

Yu, C., Z. H. Li, and N. T. Penna. 2018. "Interferometric Synthetic Aperture Radar Atmospheric Correction Using a GPS-Based Iterative Tropospheric Decomposition Model." *Remote Sensing of Environment* 204:109–121. https://doi.org/10.1016/j.rse.2017.10.038.

Zebker, H. A., P. A. Rosen, and S. Hensley. 1997. "Atmospheric Effects in Interferometric Synthetic Aperture Radar Surface Deformation and Topographic Maps." *Journal of Geophysical Research Solid Earth* 102 (B4): 7547–7563. https://doi.org/10.1029/96JB03804.

Zhan, Y. T., Y. F. Zhu, Y. J. Wang, and K. Song. 2022. "Land Subsidence Monitoring of Jiangsu Coastal Areas with High Resolution Time Series InSAR." *Science of Surveying and Mapping (In Chinese)* 47 (7): 69–76. https://doi.org/10.16251/j.cnki.1009-2307.2022.07.010.

Zhang, B. C., X. N. Liao, J. Y. Zhang, S. T. Xiong, C. S. Wang, S. B. Wu, C. H. Zhu, J. S. Zhu, X. Q. Qin, and Q. Q. Li. 2023. "Megalopolitan-Scale Ground Deformation Along Metro Lines in the Guangdong-Hong Kong-Macao Greater Bay Area, China, Revealed by MT-InSAR." *International Journal of Applied Earth Observation and Geoinformation* 122:103432. https://doi.org/10.1016/j.jag.2023.103432.

Zhang, B. W., R. Wang, Y. K. Deng, P. F. Ma, H. Lin, and J. L. Wang. 2019. "Mapping the Yellow River Delta Land Subsidence with Multitemporal SAR Interferometry by Exploiting Both Persistent and Distributed Scatterers." *ISPRS Journal of Photogrammetry & Remote Sensing* 148:157–173. https://doi.org/10.1016/j.isprsjprs.2018.12.008.

Zhang, L., X. L. Ding, Z. Lu, H. S. Jung, J. Hu, and G. C. Feng. 2014. "A Novel Multitemporal InSAR Model for Joint Estimation of Deformation Rates and Orbital Errors." *IEEE Transactions on Geoscience & Remote Sensing* 52 (6): 3529–3540. https://doi.org/10.1109/TGRS.2013.2273374.

Zhang, Y. H., H. A. Wu, M. J. Li, Y. H. Kang, and Z. Lu. 2021. "Investigating Ground Subsidence and the Causes Over the Whole Jiangsu Province, China Using Sentinel-1 SAR Data." *Remote Sensing* 13 (2): 179. https://doi.org/10.3390/rs13020179.

Zhao, Q., G. Y. Ma, Q. Wang, T. L. Yang, M. Liu, W. Gao, F. Falabella, P. Mastro, and A. Pepe. 2019. "Generation of Long-Term InSAR Ground Displacement Time-Series Through a Novel Multi-Sensor Data Merging Technique: The Case Study of the Shanghai Coastal Area." *ISPRS Journal of Photogrammetry & Remote Sensing* 154:10–27. https://doi.org/10.1016/j.isprsjprs.2019.05.005.

Zhao, Q., A. Pepe, V. Zamparelli, P. Mastro, F. Falabella, S. Abdikan, C. Bayik, et al. 2023. "Innovative Remote Sensing Methodologies and Applications in Coastal and Marine Environments." *Geo-Spatial Information Science* 27 (3): 836–853. https://doi.org/10.1080/10095020.2023.2244006.